Available online at www.sciencedirect.com
SCIENCE DIRECT®
ELSEVIER
Earth and Planetary Science Letters 244 (2006) 474–500
EPSL
www.elsevier.com/locate/epsl

Fractionation of gases in polar ice during bubble close-off: New constraints from firn air Ne, Kr and Xe observations

Jeffrey P. Severinghaus [a,*], Mark O. Battle [b]

[a] Scripps Institution of Oceanography, University of California, 9500 Gilman Dr., San Diego, CA 92093-0244, USA
[b] Department of Physics and Astronomy, Bowdoin College, 8800 College Station, Brunswick, ME 04011-8488, USA

Received 12 June 2005; received in revised form 14 January 2006; accepted 16 January 2006
Available online 28 February 2006
Editor: E. Boyle

Abstract

Gas ratios in air withdrawn from polar firn (snowpack) show systematic enrichments of Ne/N_2, O_2/N_2 and Ar/N_2, in the firn–ice transition region where bubbles are closing off. Air from the bubbles in polar ice is correspondingly depleted in these ratios, after accounting for gravitational effects. Gas in the bubbles becomes fractionated during the process of bubble close-off and fractionation may continue as ice cores are stored prior to analysis. We present results from firn air studies at South Pole and Siple Dome, Antarctica, which add Ne, Kr and Xe measurements to the suite of observations. Ne, O_2 and Ar appear to be preferentially excluded from the shrinking and occluding bubbles, and these gases therefore accumulate in the residual firn air, creating a progressive enrichment with time (and depth) in firn air. Early sealing of gases by thin horizontal impermeable layers into a non-diffusive zone or "lock-in zone" greatly enhances this enrichment. A simple model of the bubble close-off fractionation and lock-in zone enrichment fits the data adequately. The model presumes that fractionation is caused by selective permeation of gas through the ice lattice from slightly overpressured bubbles. The effect appears to be size-dependent, because Ne, O_2 and Ar have smaller effective molecular diameters than N_2, and fractionation increases strongly with decreasing size. Ne is fractionated 34 ± 2 times more than O_2 in South Pole firn air and reaches an enrichment of 90‰ in the deepest sample. The large atoms Kr and Xe do not appear to be fractionated by this process, despite the large size difference between the two gases, suggesting a threshold atomic diameter of ~ 3.6 Å above which the probability becomes very small that the gas will escape from the bubble. These findings have implications for ice core and firn air studies that use gas ratios to infer paleotemperature, chronology and past atmospheric composition.

Keywords: ice cores; trapped gases; air bubbles; noble gases; fractionation; molecular size

1. Introduction

1.1. Background

Snow accumulating on a polar ice sheet gradually compacts and sinters under its own weight to form first firn, and then ice. The firn, a layer of recrystallized and partially compacted snow, is porous and permeable to

* Corresponding author. Tel.: +1 858 822 2483; fax: +1 858 822 3310.
E-mail address: jseveringhaus@ucsd.edu (J.P. Severinghaus).

0012-821X/$ - see front matter © 2006 Elsevier B.V. All rights reserved.
doi:10.1016/j.epsl.2006.01.032

air. The air contained within the firn mixes with the atmosphere through molecular diffusion and in some circumstances, through convection [1,2]. At the base of the firn layer, which is typically 50–100 m thick in polar settings, firn air is occluded in bubbles as the firn becomes impermeable ice. Air trapped in bubbles in polar ice has been used for a wide variety of paleoenvironmental studies, principally to reconstruct the composition of past atmospheres [3,4].

Atmospheric constituents that are nearly constant in time (during the 10^6-yr period spanned by ice cores), such as the noble gases and the isotopes of N_2, have also been used to infer the local histories of climate-related processes occurring within the firn layer that overlies polar ice sheets. The most important of these processes is gravitational settling [5–7], in which heavier gas molecules are enriched towards the bottom of a column of gas in diffusive equilibrium. Gravitational enrichment increases with depth in the firn air column and with the absolute mass difference Δm between a pair of gas species, as given by the barometric equation [5]. For example, the enrichment of the $^{132}Xe/^{28}N_2$ ratio, with $\Delta m = 104$, is 104 times greater than the enrichment of $^{15}N/^{14}N$ with $\Delta m = 1$. Prior studies have used the observed enrichments of $^{15}N/^{14}N$ in air bubbles to infer past firn diffusive column thickness. This thickness is related to climatic variables of interest such as temperature and accumulation rate [8–11].

A second process that alters firn air and hence bubble air composition is thermal fractionation. A gas mixture subjected to a temperature gradient will tend to unmix, with heavier components generally migrating towards colder regions [12]. Thermal fractionation of air in the firn is driven by transient temperature gradients that arise from seasonal temperature change [13] or during the several hundred years following rapid climate changes [14–16]. The resulting isotopic signal is captured in bubbles in ice and permits reconstruction of the magnitude and rapidity of past climate change [17].

Here we concentrate on a third process that alters firn and bubble air composition: the preferential exclusion of Ne, Ar and O_2 during bubble close-off. Ice core bubble air is typically depleted in Ar/N_2 and O_2/N_2 relative to atmospheric values, with the Ar depletion typically half that of the O_2 depletion [2,6,8,18]. The fact that Ar is heavier than N_2 and O_2, yet has intermediate depletion, argues against a mass-dependent fractionation process, but is consistent with the ordering of molecular sizes [5]. Typical values for $\delta O_2/N_2$ in well-preserved ice samples are −4‰ to −8‰ [18]. Some very large depletions with this size-dependent signature observed in certain ice cores can probably be attributed to artifactual gas loss during core retrieval or handling (e.g., the deep Byrd core, with $\delta O_2/N_2 = -200‰$ and $\delta Ar/N_2 = -100‰$) [18]. Poor core quality is often associated with low O_2/N_2 [19] and long storage of samples in freezers at −25 °C has been shown to cause depleted O_2/N_2 [20,21]. However, firn air studies show that some in situ (natural) size-dependent fractionation process must also occur [2]. Furthermore, Bender [19] has recently shown that Vostok ice core O_2/N_2 correlates strongly with local insolation, a relationship confirmed by Dome Fuji O_2/N_2 [20]. These latter studies clearly imply a natural O_2/N_2 fractionation at bubble close-off.

In support of this conclusion, we report measurements of noble gas ratios, O_2 and isotopes of N_2 in air withdrawn from the firn at Siple Dome and South Pole, Antarctica. The data show large enrichments of O_2/N_2 (up to 10‰), Ne/N_2 (up to 90‰) and Ar/N_2 (up to 3‰) in the transitional region where firn becomes ice. Kr/N_2 and Xe/N_2 show no such enrichment, providing an important constraint on fractionation mechanisms. Bubble air composition is depleted in O_2/N_2 in a complementary fashion, as would be expected by mass balance if the segregation process occurred during bubble close-off [2]. However, the magnitude of the observed depletion in ice samples is often a factor of 2–4 greater than predicted by mass balance; we discuss this discrepancy further below. We also show that the Ne/N_2 and O_2/N_2 enrichments are well correlated and discuss implications for paleoenvironmental studies of gas ratios in polar firn and ice.

1.2. The firn–ice transition and "lock-in" zone

Initial density differences in snow deposited at the surface in summer and winter appear to be preserved through the entire densification process in the firn [22]. Thus, higher-density winter layers become impermeable before lower-density summer layers as the firn turns to ice. These layers allow horizontal movement within each summer layer while preventing most vertical movement [1,2,7,9,22–24]. The result is a vertical region in the firn, referred to as the "lock-in zone", at the transition between firn and ice (Fig. 1). While some authors [2] originally thought that vertical movement was completely blocked in this zone, we suggest in this paper that widely spaced leaks permit some gas to escape upward. The zone is defined above by the onset of impermeable winter layers and below by the complete absence of open pores (the firn–ice transition). Large volumes of air can be drawn from the open summer layers within the lock-in zone.

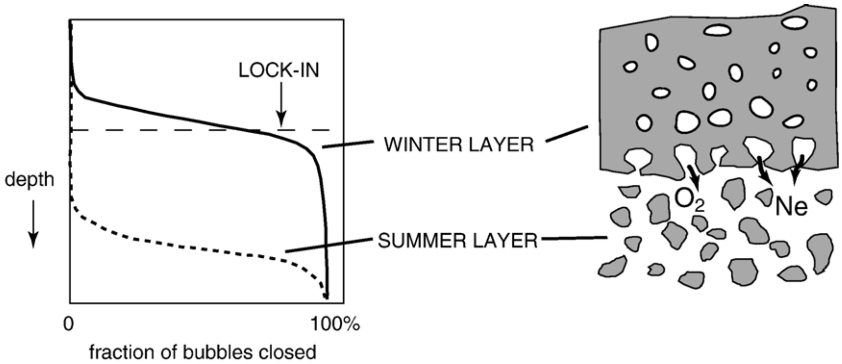

Fig. 1. Schematic of sealing of firn air in the lock-in zone prior to complete bubble close-off and how close-off fractionation produces progressive enrichment of small molecules in air in the remaining open firn pores.

The lock-in zone may be 5 to 10 m thick in polar settings. Because vertical movement of gas is restricted in the lock-in zone, the progressive gravitational enrichment of $^{15}N/^{14}N$ with depth ceases and $^{15}N/^{14}N$ is essentially constant [2]; the same is true for $^{40}Ar/^{36}Ar$ (Fig. 2). The lock-in zone is notable in that the age of its air increases at the same rate as the age of the ice surrounding it [2], which makes air from the bottom of the lock-in zone substantially older than air in the diffusive column. This source of "old air" has attracted much attention as an archive of the past atmosphere, since it has the potential to produce samples of air that are much larger and freer of contaminants than those recovered from bubbles trapped in ice cores.

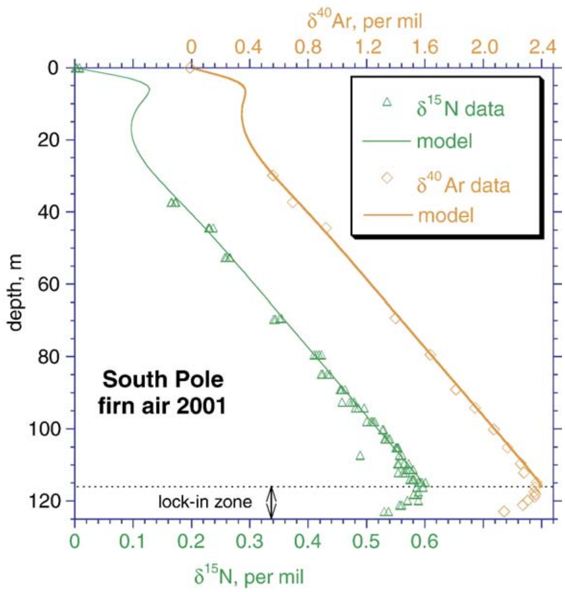

Fig. 2. $\delta^{15}N$ and $\delta^{40}Ar$ profiles from the firn at South Pole. Note the inflection point near the bottom of the profiles. In this region, gases no longer mix vertically and are effectively "sealed" into isolated horizontal layers in the lock-in zone. Hence, gravitational enrichment of the heavy isotopes cease and (absent other processes) we would expect the values to be constant in this interval. The observed decrease implies a small fractionation during sampling, which we show to be mass-dependent (see Section 5). The model convective zone has the effect of shifting the whole model curve down by about 2 m, without changing the slope.

2. Methods

Air was withdrawn from the firn following the method pioneered by Schwander et al. [1], as modified by Bender et al. [25] and Battle et al. [2]. A hole was drilled to the desired depth and a 4-m long natural rubber packer was inserted and inflated to form a seal in the hole. Air was pumped from the ~10-cm high space below the packer, from two separate openings separated by a horizontal stainless steel baffle nearly as wide as the hole. The upper opening was pumped to waste at a flow rate of 10 l min^{-1}, to eliminate any air that may have leaked out of or around the packer. The sample was taken from the lower opening at 2 l min^{-1} and, because the lower opening was below the baffle, the sample should not have come into contact with the packer. Lines were flushed for at least 10 min before sampling, and samples were passed through a P_2O_5 dessicant and stored in 2-l flow-through glass flasks sealed with Louwers-Hapert valves and viton o-rings [25]. Flasks were also filled after pumping ~1000 l of air from the firn at several depth to look for changes in composition during the course of sampling. No such changes were observed.

Flasks from Siple Dome were analyzed at the University of Rhode Island on a Finnigan MAT 251 mass spectrometer in dual-collector mode for O_2/N_2, $^{15}N/^{14}N$ and ^{18}O of O_2 as described in Bender et al. [26,27]. South Pole flasks were analyzed at Princeton on a Finnigan Delta Plus XL mass spectrometer at least in triplicate for O_2/N_2, $^{15}N/^{14}N$ and $^{40}Ar/N_2$ as described by Bender et al. [27]. Samples were analyzed against a dry air standard and are reported here against samples of surface air. Pooled standard deviations from the means of replicate flasks are 0.004‰, 0.003‰ and 0.007‰ for O_2/N_2, $^{15}N/^{14}N$ and $^{40}Ar/N_2$, respectively.

Subsets of the Siple Dome flasks ($n=13$ out of 45 total) and South Pole flasks ($n=20$ out of 54 total) were then analyzed for noble gases. Selection of the subset was arbitrary except that flasks with anomalous $^{15}N/^{14}N$ were avoided. Noble gases were run on a Finnigan MAT 252 mass spectrometer at SIO for $^{40}Ar/^{36}Ar$ and $^{40}Ar/^{38}Ar$ in dual-collector mode, and $^{84}Kr/^{36}Ar$ and $^{132}Xe/^{36}Ar$ by peak-jumping (with mass spectrometry as described by Severinghaus et al. [11]). Samples were prepared by exposing 40 cc STP to a Zr/Al getter at 900 °C for 10 min to destroy all the reactive gases, followed by 2 min at 300 °C to remove H_2. This left ~0.4 cc STP of residual noble gas (primarily argon). This gas was cryogenically concentrated at 4 K into a vessel, then admitted into the mass spectrometer after allowing the vessel contents to mix internally for 45 min at room temperature to insure homogeneity. South Pole flasks were also analyzed for $^{22}Ne/^{36}Ar$ by peak-jumping. We do not have Ne data for Siple Dome and the samples have been consumed. Samples were run against aliquots of a standard gas mixture of commercially obtained Ne, Ar, Kr and Xe. The mass/charge 44 beam was monitored to assure insignificant isobaric interference with ^{22}Ne from doubly charged CO_2.

The 13 Siple Dome flasks were run in duplicate (9 flasks) or triplicate (4 flasks) aliquots. One flask was run a third time because of a gross procedural error and results from the affected aliquot were rejected. The remaining three flasks were run a third time because of poor reproducibility in the first two aliquots' results. From these, one $^{132}Xe/^{36}Ar$ measurement (from 30.55 m depth) was rejected on the basis of poor agreement with the other two measurements. In the remaining Siple Dome data, the pooled standard deviation from the mean of replicate aliquots (reproducibility) was 0.004‰ and 0.009‰ for $^{40}Ar/^{36}Ar$ and $^{40}Ar/^{38}Ar$, and 0.10‰ and 0.26‰ for $^{84}Kr/^{36}Ar$ and $^{132}Xe/^{36}Ar$, respectively. South Pole flasks were initially run in duplicate, but eight aliquots were rejected and re-run because sample pressure was discovered to have been inadequate, due to low pressures in the flasks. One aliquot was rejected and re-run due to the presence of O_2 and N_2, indicating a leak. The remaining data set consisted of 17 flasks run in duplicate and 3 flasks run in triplicate. These three were run a third time because of poor agreement of replicates; however, none were rejected. The pooled standard deviation of the remaining 43 points was 0.006‰ and 0.007‰ for $^{40}Ar/^{36}Ar$ and $^{40}Ar/^{38}Ar$, and 0.09‰, 0.42‰ and 0.35‰ for $^{84}Kr/^{36}Ar$, $^{132}Xe/^{36}Ar$ and $^{22}Ne/^{36}Ar$, respectively.

Results are presented in the customary delta notation, the per mil deviation of the sample ratio R_{SA} from a standard R_{ST}, which for inert gases is the free troposphere.

$$\delta = [R_{SA}/R_{ST} - 1] \times 10^3‰ \tag{1}$$

For most gas pairs, the following abbreviations in the notation are used: $\delta^{15}N$ for $^{15}N/^{14}N$, $\delta^{40}Ar$ for $^{40}Ar/^{36}Ar$, $\delta Ar/N_2$ for $^{40}Ar/^{28}N_2$, $\delta Kr/N_2$ for $^{84}Kr/^{28}N_2$, $\delta Xe/N_2$ for $^{132}Xe/^{28}N_2$, $\delta Ne/N_2$ for $^{22}Ne/^{28}N_2$ and $\delta O_2/N_2$ for $^{32}O_2/^{28}N_2$. For Kr, Xe and Ne, we calculate the ratios to N_2 after measurement, using the observed $^{40}Ar/^{28}N_2$:

$$\delta Kr/N_2 = \{[\delta^{84}Kr/^{36}Ar\ 10^{-3} + 1]/[\delta^{40}Ar\ 10^{-3} + 1] \times [\delta Ar/N_2 10^{-3} + 1] - 1\} 10^3‰ \tag{2}$$

with analogous treatment of Xe and Ne. Precision of $\delta^{40}Ar$ and $\delta^{40}Ar/N_2$ was much better than that of Kr, Xe and Ne, so this calculation did not affect the precision noticeably. Results of the $^{40}Ar/^{38}Ar$ measurements add little new information so are not presented here, but are available on request.

3. Model of the bubble close-off fractionation and lock-in zone

We have built a model describing the close-off of bubbles, the diffusion of gases within the firn and exchange with the atmosphere, and the evolution of temperature and gas composition in the open pores and bubbles in time and space. A detailed description of the model architecture is given in Appendix A.

3.1. Permeation model

The model is based upon the hypothesis that the close-off fractionation occurs because the ice lattice is slightly permeable to gases, with permeability being much higher for some gases than others. The hypothesis of differential permeability through the lattice was recently advanced by Ikeda-Fukazawa et al. [21] to explain the observation that O_2/N_2 ratios in air-clathrate-bearing ice samples decrease over several years of storage in a freezer at 248 K. The fractionation occurs because the permeation coefficient of O_2 in ice is a factor of 3 larger than that of N_2 [21]. We consider the possibility that a similar process occurs in Nature during bubble close-off, albeit with much lower pressure differences and much shorter diffusion path lengths.

The newly formed bubbles are undergoing compression [28,29], creating a pressure difference between the bubble and the adjacent open pores, which are assumed to remain at ambient pressure. We propose that this pressure difference drives a permeation flux of O_2, N_2 and other gases through the thin ice wall of the newly formed bubble into the adjacent open pore (Fig. 3). The model uses the permeation coefficients of Ikeda-Fukazawa et al. [21], which are strongly temperature-dependent. The flux of gas through the ice is assumed to be given by Fick's First Law as the product of the concentration gradient and the diffusivity:

$$\begin{aligned} j_n &= D_n \partial C_n / \partial z \\ &= D_n X_n \partial p_n / \partial z \approx D_n X_n \Delta p_n / z_\mathrm{w} \quad \mathrm{mol\ m^{-2}\ s^{-1}} \end{aligned} \qquad (3)$$

where j_n is the flux of gas n per unit area, D_n is the diffusivity of gas n in the ice lattice, C_n is the dissolved concentration of gas n in the lattice, z is distance through the ice wall, X_n is the solubility of gas n in ice, p_n is the partial pressure of gas n, Δp_n is the partial pressure difference across the wall and z_w is the wall thickness (Fig. 3). The product of the diffusivity and solubility $D_n X_n$ is the permeation coefficient and as an example has a value for O_2 of 1.3×10^{-20} mol m^{-1} s^{-1} Pa^{-1} at 248 K [21]. It is recognized that both the pressure difference and the wall thickness will be variable functions of time. The total flux from a single bubble at a given instant is therefore:

$$J_n = D_n X_n \Delta p_n(t) / z_\mathrm{w}(t) A \qquad \mathrm{mol\ bubble^{-1}\ s^{-1}} \qquad (4)$$

where A is the effective area of the wall available for diffusion and t is time. Unfortunately, the pressure difference, wall thickness and area are unknowns. To proceed with a minimalist model that still has some physical meaning, we make the following four simplifying assumptions.

(1) The wall thickness increases linearly with the change in porosity, with a slope given by γ, an unknown constant:

$$z_\mathrm{w} = \gamma(s/s' - 1) \qquad \mathrm{m} \qquad (5)$$

where s is the porosity when the bubble closed and s' is the porosity at any later time. This assumption is chiefly made for mathematical simplicity and has no real justification other than that firn metamorphism should increase the wall thickness with time, and firn metamorphism also causes a decrease in the porosity with time, so wall thickness should be generally related to the porosity change.

(2) Bubble compression occurs in proportion to the change in total porosity. This is a reasonable assumption, because the load is much larger than bubble pressure at this stage, so bubbles should compress just as much as open pores. This implies that the pressure in the bubble and hence the pressure difference increases according to:

$$\Delta p_n = x_n P(s/s' - 1) \qquad \mathrm{Pa} \qquad (6)$$

where P is the barometric pressure in the open pores and x_n is the mole fraction of gas n in the bubble. The changes in mole fraction are small enough (<1%) that they may be neglected and the effect of the permeation flux on bubble pressure is also neglected. Substituting Eqs. (5) and (6) into Eq. (4), the $(s/s' - 1)$ terms cancel, making the flux proportional to $x_n P/\gamma$. Another way of saying this is that the wall thickens as the pressure increases, so the flux remains constant. The physical meaning of γ may be thought of as the wall thickness when bubble pressure is twice ambient.

(3) The effective area of the wall available for diffusion A is constant. Although bubble size does vary temporally and spatially, the ratio of area A to the volume of the bubble governs the calculated flux from an ensemble of bubbles (see Appendix A). This ratio is assumed to be constant. For roughly spherical bubbles,

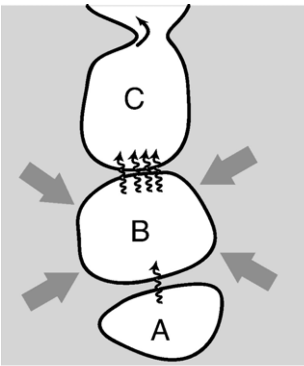

Fig. 3. Schematic of our idealized model for permeation-related fractionation during bubble close-off. Bubble A is in a more advanced stage of compression than bubble B, as is bubble B relative to bubble C, which has not yet closed off. Bubble pressure therefore decreases from A to B and from B to C. It is assumed that most fractionation occurs because of gas permeation through the ice lattice from bubble B to bubble C, through the thin wall of ice separating the two. Gases are assumed to be free to diffuse quickly into the open firn from bubble C. No net fractionation of the bulk ice occurs by the permeation from bubble A to bubble B, because the fractionated gases simply accumulate in bubble B. The model also assumes that bubble C will close off when a constant amount of compression has occurred (5% in the present model) relative to the porosity at the moment that the adjacent bubble (bubble B) closed off, on average.

area will change as the radius squared, while volume depends on the radius cubed, so this approximation is good to leading order.

(4) Net fractionation only occurs from bubbles that are immediately adjacent to open pores. When the bubble is separated from open pores by one or more other bubbles, no net fractionation of the bulk ice occurs, because the fractionated gases simply accumulate in the adjacent bubble. For the purpose of this model, we suppose that on average the adjacent bubble closes after some constant critical value of porosity change is reached $(s/s'-1)_c$. Hence, net fractionation will terminate after this critical porosity change is achieved. The time required for this critical porosity change is the critical time t_c, which is related in a known way to $(s/s'-1)_c$ by the ice accumulation rate $\dot{b}$ and the density profile ρ. This gives the model a dependence on accumulation rate; more fractionation should occur at low-accumulation sites because there is more time for the gas to escape.

$$J_n = D_n X_n x_n P/\gamma A \quad \text{for } t < t_c(\dot{b}, \rho, (s/s'-1)_c) \tag{7}$$

$$J_n = 0 \quad \text{for } t \geq t_c(\dot{b}, \rho, (s/s'-1)_c) \ \text{mol bubble}^{-1}\ \text{s}^{-1} \tag{8}$$

The time-integrated flux of gas contributing to net fractionation, or the effective total moles of gas lost from a bubble, is therefore:

$$\begin{aligned} \text{gas lost} &= D_n X_n x_n P/\gamma A t_c(\dot{b}, \rho, (s/s'-1)_c) \\ &\approx D_n X_n x_n P/\gamma A (s/s'-1)_c \\ &\quad \times \partial t_c / \partial (s/s'-1)_c. \end{aligned} \tag{9}$$

The amount of gas lost is thus proportional to $D_n X_n x_n$. The only unknowns in (9) are the constants A, γ and $(s/s'-1)_c$ (the derivative may be determined independently from density and accumulation rate data; see Appendix A). We lump these three unknowns into a single arbitrary constant and adjust it to fit the firn air data. The constant has units of length and may be thought of as a characteristic length scale. It may be thought of as the area available to diffusion divided by the thickness through which diffusion must occur (normalized to a pressure difference equal to ambient pressure), times the average porosity decrease between closing of adjacent bubbles. This length scale is arguably independent of gas type, accumulation rate and temperature. Thus, its hypothesized constancy should be testable by comparisons with data for different gases, and different firn sites with differing temperature and accumulation rate. The constant should have physical meaning, although the model is highly simplified and subsequent attempts will surely improve on it.

As will be seen below, fits to the data suggest a value of 5 μm for the length scale. This could correspond, for example, to $A = 10^{-7}$ m^2, $\gamma = 10^{-3}$ m and a critical porosity change of 0.05 or 5%. This would be equivalent to a circular wall with a diameter of 0.35 mm, an average wall thickness during fractionation of 25 μm and an average bubble overpressure during fractionation of 2.5% over ambient pressure. For practical reasons, the numerical model explicitly uses a critical value of 0.05, as detailed in Appendix A.

Because of the strong temperature dependence of the permeation coefficients [21], the model would predict ~4× as much gas loss at Siple Dome temperature than at South Pole temperature for a given accumulation rate. The higher accumulation rate at Siple Dome reduces this effect to roughly a factor of 2. As shown below, this factor of 2 is consistent with the observational data; a length scale of 5 μm fits the O_2/N_2 data at both sites fairly well.

3.2. Firn air transport model

The permeation model just described is embedded in a firn gas and heat transport model, which is a one-dimensional advection–diffusion model based on earlier work of Schwander et al. [1]. The model is forced at the surface by known or inferred atmospheric histories of CO_2 and O_2, and by measured temperatures. The amount of gas enclosed in each part of the model per unit time is parameterized from measured closed porosity data (see Appendix A) and the assumption of steady state in the closed porosity profile. The lock-in zone is treated as a simple downward advection of gas, with values being transferred down by one annual layer each year and fractionated. Fractionation of the remaining gas in the open pores is computed by conservation of mass. A small amount of gas is expelled from the lock-in zone through a viscous leak (i.e., without fractionation) into the open firn column above, as required by conservation of mass and the assumption that the air in open pores remains at ambient pressure.

The model is calibrated for each site in a series of four steps, against observed quantities, in a sequence that reflects the independence of the constraints. We avoided introducing unconstrained free parameters in the model, except for the length scale, so that the model cannot be arbitrarily tuned to produce any result.

a. Model density is obtained from curve fits to observed density–depth profiles at each site.

b. Model closed porosity is obtained from a fit to measured closed porosity vs. density data from Greenland Summit (see Appendix A).
c. Model convective zone is adjusted to match $\delta^{15}N$ and $\delta^{40}Ar$ data (Fig. 2). The convective zone is a zone near the surface of the firn in which vigorous convective mixing by windpumping [30] reduces the magnitude of gravitational fractionation, shifting the whole $\delta^{15}N$ or $\delta^{40}Ar$ profile downward [8]. These gas species are independent of atmospheric change and are only very weakly sensitive to firn diffusivity.
d. Effective firn diffusivity vs. depth is adjusted to match the model CO_2 profile to the data (see Appendix A), taking advantage of the strong constraint afforded by the anthropogenic transient [31]. The lock-in depth (LID) is identified by this process, and is confirmed by the $\delta^{15}N$ and $\delta^{40}Ar$ data. The LID is effectively where diffusivity goes to zero and the gas ages rise at the same rate as the surrounding ice.

After the model was calibrated for a particular site, the depth profile of each gas was calculated using the same site-specific parameters, while allowing the length scale to vary to match observed gas data in the lock-in zone. The length scale derived for the lock-in zone is also used to describe exclusion from bubbles forming in the open firn. The quality of fit in the lock-in zone reflects the constancy of the fractionation and the quality of the fit in the lower part of the open firn reflects the similarity between fractionation in the firn and the lock-in zone.

We do not expect the exact value of the length scale to be particularly meaningful, as it may be affected by sampling bias or flaws in the closed porosity parameterization and model assumptions (see Appendix A). Nonetheless, the ratios of observed fractionation for different pairs of gas species should be related indirectly to the ratios of the permeation coefficients, as the aforementioned limitations cancel.

We are aware of several shortcomings of our model. First among them is the highly simplified nature of the permeation model. The time history of permeation contributing to fractionation is likely more complex than we have assumed. Future work will surely improve on the highly schematic treatment of bubble close-off; the present model serves mainly as an illustration of one minimally complex yet physically plausible method for condensing all unknown parameters into a single adjustable constant that may be fit to data. Other approaches may be successful, and we have not explored all possibilities. A second shortcoming is that the model produces ice with a bubble O_2/N_2 ratio higher than that typically observed in ice samples taken by coring (see Appendix A). However, part of this discrepancy may be caused by O_2 loss from the ice samples during coring and storage [18], and it is not clear at present what the true value of O_2/N_2 is in ice. A third weakness is the absence of downward advection of gases in the open firn due to the accumulation of snow. This omission is satisfactory at slow accumulation sites like South Pole and Siple Dome, but is problematic elsewhere [32]. In the extremely low-diffusivity region just above the lock-in, this may lead to overestimates of the diffusivity. Similarly, the gravitational enrichment in the lower part of the firn is slightly overestimated in the model. In Nature, the gas near the lock-in is advected downward during the time required for gas to diffuse from the surface, and full diffusive equilibrium is never established. Finally, measured closed porosity data would ideally be used at each site; however, these are not yet available.

4. Observations

To isolate the close-off fractionation for closer study, it is helpful to compute gravitationally corrected values [2,6,11,19]. This is done by subtracting $\delta^{15}N \times \Delta m$ (for O_2/N_2 and Ar/N_2) or $\delta^{40}Ar \times \Delta m/4$ (for all other gases), where Δm is the mass difference of the gas pair being corrected:

$$\delta_{gravcorr} = \delta_{measured} - \delta^{15}N_{measured} \times \Delta m \quad ‰. \tag{10}$$

Fractionation may also result from a temperature gradient (thermal fractionation) [12]. Fortuitously, Eq. (10) corrects well for this process in the case of O_2/N_2. This is because the thermal diffusion effect for O_2/N_2 is almost exactly four times larger than for $\delta^{15}N$ at South Pole temperatures [13]. Thermal fractionation for Ar/N_2, Kr, Xe and Ne deviates somewhat from the Δm scaling [33], but in all cases the discrepancy is less than the measurement error. The $\delta^{15}N$ (rather than $\delta^{40}Ar$) is used to correct O_2/N_2 and Ar/N_2 because these three gas pairs are measured together in the laboratory, so any small artifactual fractionation introduced at this step would be corrected to first order. In summary, after making the empirical correction given in Eq. (10), variations in firn air composition with depth should reflect only fractionation due to permeation and sample collection, or (in the case of O_2/N_2) evolving atmospheric composition.

Measured O_2/N_2 ratios vs. depth in South Pole firn are shown in Fig. 4, gravitationally corrected. These show a gradual increase with depth through most of the firn, attributable to anthropogenic change due to fossil fuel burning. Starting 8–10 m above the top of the lock-

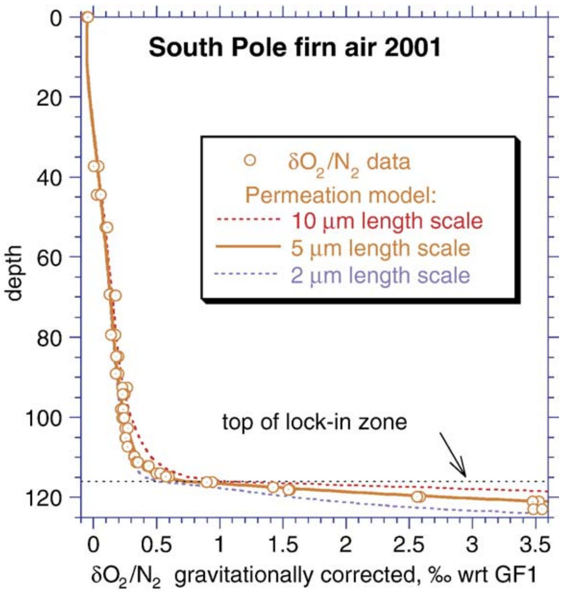

Fig. 4. Firn air O_2/N_2 profile taken in 2001 at South Pole, gravitationally corrected. The sharp rise in O_2/N_2 in the bottom 8 m of the firn, which is the lock-in zone, coincides with a sharp drop in CO_2 and CH_4. The large enrichment of O_2/N_2 suggests a fractionating process that occurs within the sealed horizons of the lock-in zone, creating the progressive enrichment with depth (and time). Note that O_2/N_2 is also enriched in the 10 m above the lock-in zone, which reflects an uphole O_2 flux from permeation from closing bubbles. Permeation model results appear to fit the data with a single free parameter (the length scale, see Section 3.1).

in zone, there is a sharp non-linear increase reflecting some process other than gravitational enrichment. We follow earlier authors [2,11] in attributing this O_2/N_2 increase to fractionation during bubble close-off, with progressive accumulation of O_2 in the trapped residual firn air as in a Rayleigh-type distillation. The O_2/N_2 profile was simulated by tuning the model length scale to fit the data in the lock-in zone. At shallower depths, model diffusivities were found by independent calibration to CO_2 data, so the gradients produced by the model should accurately reflect the uphole flux of O_2 via Fick's First Law [2]. The good agreement of model and data in the diffusive firn therefore suggests that the model produces about the right amount of uphole O_2 flux.

Gravitationally corrected Ne/N_2 at South Pole is shown in Fig. 5. The large enrichment in the lock-in zone reaches +90‰ in the deepest sample [34]. Furthermore, a substantial uphole flux is implied by the gradients in the 30 m above the lock-in horizon; the firn appears to be expelling substantial neon to the atmosphere. The profile was modeled using the length scale (5 μm) found from the O_2/N_2 data as described above, giving a good fit to the data. In particular, the agreement shows that the model correctly predicts the uphole flux of Ne. More generally, the good fit of the model to the data supports the notion that fractionated gases accumulate with time in the lock-in zone. Because atmospheric Ne/N_2 is constant in time, Ne is in a sense a "simpler" gas than O_2. It isolates the physical factors acting on O_2/N_2 in the firn without complications from biogeochemistry.

Another approach to remove the complication of biogeochemistry is to correct the O_2/N_2 data for atmospheric change. This is done in Fig. 6 by running the model with and without atmospheric change (see Appendix A for the assumed atmospheric history of O_2/N_2), and subtracting the difference between the two results from the data. When plotted vs. O_2/N_2 corrected for atmospheric change and gravitational enrichment, Ne/N_2 in the lock-in zone shows an excellent correlation ($R^2=0.992$; Fig. 6A). This correlation suggests that a single physical process is causing the fractionation, since multiple processes would probably lead to different slopes in the O_2/N_2–Ne/N_2 relationship at different stages of the densification process. The slope found by linear regression is 34.0 ± 1.5 (95% confidence interval). Including the uncertainty associated with our assumed atmospheric O_2 history, we arrive at an error of ±2 for this slope value. Further firn air studies are needed to see if the value of 34 is a constant, or varies from site to site. The tightness of the correlation raises

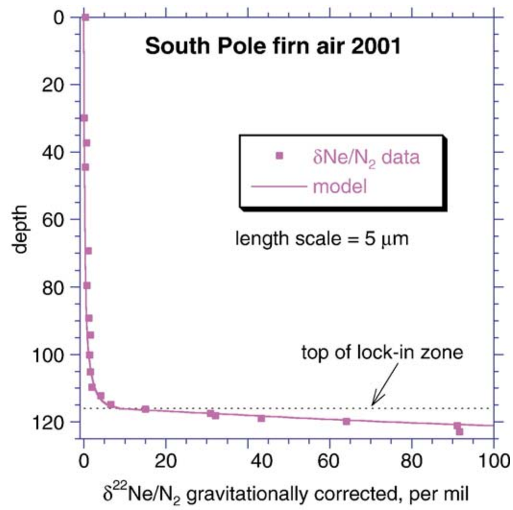

Fig. 5. Neon–N_2 ratio in South Pole firn air. Notice the striking enrichment of neon in the lock-in zone, in addition to the up-hole neon flux implied by the gradient in the ~30 m above the lock-in zone. This strongly suggests a size-dependent fractionation during bubble close-off, because neon is a small atom. The model neon permeability was arbitrarily tuned to fit the firn air data, because no reliable neon permeability data are available to our knowledge. A value 23× that of O_2 was found.

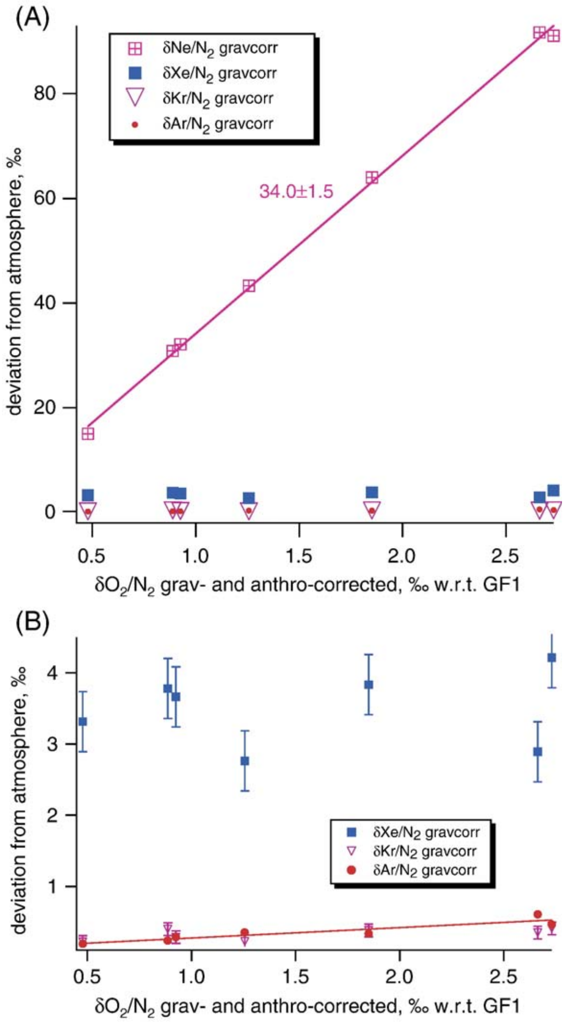

Fig. 6. Noble gases plotted vs. O_2/N_2 in the lock-in zone at South Pole, below 116 m. All data are corrected for gravitational enrichment and O_2/N_2 is corrected for anthropogenic change in the atmosphere. Correction for anthropogenic effects was done by subtracting from the data the difference between model O_2/N_2 values with and without atmospheric change. (A) Neon increases with depth in the lock-in zone 34.0 ± 1.5 times more than O_2 (95% confidence interval), implying that neon is affected by the close-off fractionation 34 times more than O_2. No significant trend is seen in Kr and Xe, implying that these gases are not fractionated from N_2 during close-off (Kr vs. O_2 regression slope = +0.054 ± 0.081, 95% confidence interval; Xe vs. O_2 regression slope = +0.08 ± 0.67, 95% confidence interval). (B) Expanded view, showing weak covariation of Ar with O_2 in the South Pole lock-in zone (slope = 0.145 ± 0.07, 95% confidence interval), and absence of trends in Kr and Xe. Error bars show pooled standard deviation of replicate analyses from the flask mean.

hopes that eventually Ne might be used to correct firn air and ice core O_2/N_2 records for physical fractionation effects.

In contrast to Ne, gravitationally corrected Kr/N_2 and Xe/N_2 exhibit no significant trends with increasing O_2/N_2 in the lock-in zone, while Ar/N_2 shows only a weak positive relationship (Fig. 6B). From these observations, we conclude that the close-off fractionation depends on molecular diameter and significantly affects only those species with a diameter less than some threshold value. Our reasoning follows.

Effective atomic diameters during intermolecular collisions may be inferred from observed viscosity data [35] (Table 1). The degree of close-off fractionation decreases from Ne to O_2 to Ar, in order of increasing diameter. However, neither Kr nor Xe shows any sign of close-off fractionation. Because Kr has a diameter of 3.65 Å (Table 1) and Ar has a diameter of 3.54 Å, our results imply the existence of an effective threshold size at ~3.6 Å. Above this threshold, gases appear to not be significantly affected by the close-off fractionation and, below it, gases observed to date are without exception affected by size-fractionation (Table 1). Furthermore, Xe has a substantially larger effective atomic diameter than Kr (4.05 vs. 3.65 Å). If close-off fractionation affected Kr or Xe, it should do so differentially between

Table 1
Molecular size and observed fractionation in firn air

Gas	Collision diameter [a] (from viscosity data), 10^{-10} m	Observed fractionation from N_2 [b] (relative to O_2/N_2), R_{oe}
Xe	4.047	0
CO_2	3.941	0 [c]
N_2O	3.828	
N_2	3.798	–
CH_4	3.758	0 [c]
CO	3.690	
Kr	3.655	0
Ar	3.542	0.33 (0.145 for South Pole)
O_2	3.467	1
Ne	2.820	34
H_2	2.827	
He	2.551	

[a] The number of significant figures are as given by [35] although it is not known to us if this number accurately represents the uncertainty. Also, we note that effective diameter depends on the nature of both molecules in a collision. In our case, the relevant collisions are between a gas and a water molecule in the ice lattice, so the values given here (which were measured in pure gases) may have limited relevance [35].

[b] Defined as the observed slope of a plot of lock-in zone $\delta n/N_2$, where n is the gas in the first column, vs. $\delta O_2/N_2$ (for example, Fig. 6). All gases are corrected for gravitational fractionation and atmospheric change. Also called the ratio of enrichment R_{oe} (this study).

[c] Inferred from agreement of firn air observations and bubble air observations [23,24]. The precision of these measurements is much lower than for the other gases in this study, so these measurements only place upper limits on the magnitude of possible fractionation. These limits indicate that close-off fractionation is not significant for the (large) atmospheric variations in CO_2 and CH_4. We cannot rule out the possibility of smaller effects of order 1‰ based on present data.

Kr and Xe because of their different diameters. The fact that they both appear to have no trend in the lock-in zone lends additional support to the interpretation that Kr and Xe are not significantly affected by size-fractionation.

Similar results are seen for Siple Dome firn air, where samples were taken in 1996 as part of the Siple Dome deep coring effort [13]. Siple Dome is a much warmer site (−25 °C; Table A1) than South Pole, with more heterogeneous firn structure [36], so it should provide a challenging test of the hypothesis including the inferred length scale and close-off parameterization. The CO_2 data provide tuning for effective diffusivities as at South Pole (see Appendix A). Measured $\delta^{15}N$ (Fig. 7) and $\delta^{40}Ar$ (not shown) have similar features as South Pole: a shallow near-surface convective zone 1–2 m deep and a lock-in zone ~8 m thick in which gravitational fractionation ceases and $\delta^{15}N$ and $\delta^{40}Ar$ decrease slightly with depth. The derived LID (49 m) is much shallower than at South Pole owing to the fact that warm temperature causes rapid metamorphism and a thin firn layer [37]. Within this lock-in zone, $\delta^{40}Ar$ is fractionated 4× as much as $\delta^{15}N$. The only surprise in the Siple Dome data is that the apparent mass-dependent fractionation of $\delta^{15}N$ and $\delta^{40}Ar$ in the lock-in zone is an order of magnitude smaller than at the South Pole (compare Figs. 2 and 7).

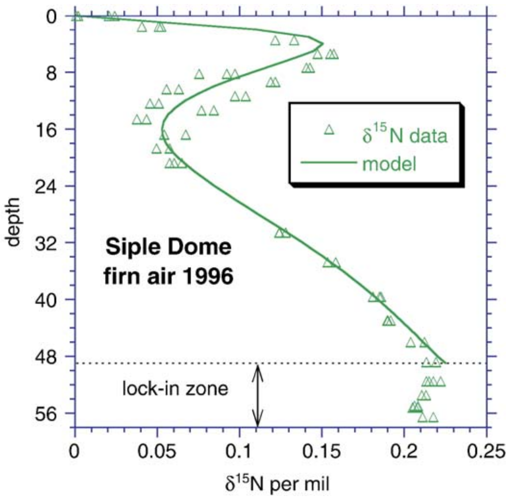

Fig. 7. Siple Dome $^{15}N/^{14}N$ profile. The inflection point in the data at 49 m confirms the depth of the lock-in horizon found from CO_2 data. The slight decrease of $\delta^{15}N$ with depth in the lock-in zone is one-third that at South Pole, which is consistent with the hypothesis that this decrease is due to a sampling artifact. Further support is provided by the fact that the deepest sample, with higher $\delta^{15}N$, was from a high-permeability layer, which allowed sampling with less vacuum than the overlying samples. The shallow data (<20 m) are discussed in [13] and will not be considered here.

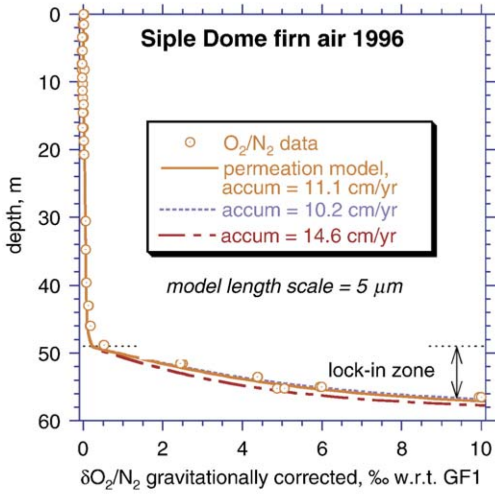

Fig. 8. Firn air O_2/N_2 profile from Siple Dome, Antarctica. As at South Pole, O_2/N_2 ratios are progressively enriched with depth in the lock-in zone. The model uses the same value of the length scale found at South Pole, 5 μm, and the same closed porosity parameterization, so the good fit of model and data at this relatively warm site (−25 °C) constitutes a successful test of the permeation model. Average accumulation rate over the firn column of 11.1 cm/yr is found from the published time scale [57].

O_2/N_2 shows similar trends in the lock-in zone at Siple Dome as at South Pole, reaching values of +10‰ in the deepest sample (Fig. 8). The fit of the model to the data is again very good, although O_2/N_2 values are somewhat underestimated. This observation suggests that despite the fourfold larger permeability due to the warmer temperature, the model still underestimates the effective fractionation. This observation also implies that fractionation during close-off varies from site to site, rather than being a constant. The slight upward curvature evident in the model lock-in zone O_2/N_2 is consistent with the idea that fractionated gas accumulates progressively (as in a Rayleigh distillation) combined with a linear increase in closed porosity with depth. Thus, each year's bubble closure takes a progressively larger fraction of the remaining gas than in the previous year. While the similarity of curvature in model and data is encouraging, we recognize that other physical phenomena could lead to the observed curvature.

When Ar/N_2 is plotted vs. O_2/N_2, a tight correlation (slope = 0.33, $R^2 = 0.997$) is seen in the lock-in zone (Fig. 9). This observation supports the hypothesis that Ar and O_2 are both fractionated by the close-off and suggests that Ar is 33% as affected as O_2. We do not understand why the slope is larger here than at South Pole (0.145), nor do we understand why the value of 0.33 is smaller than the value of 0.5 observed for Ar vs. O_2 fractionation associated with gas loss during ice core

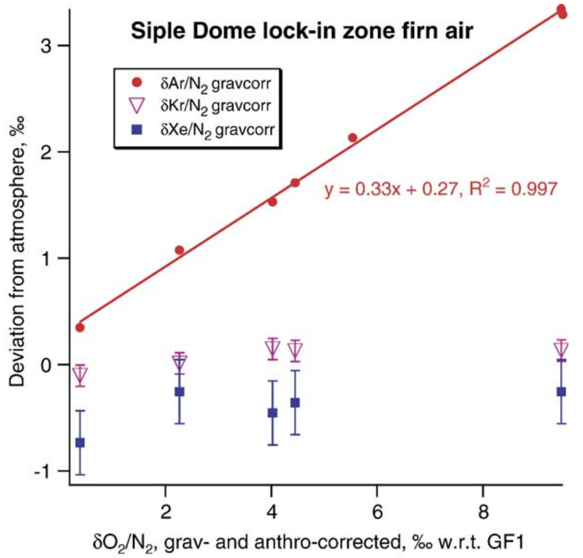

Fig. 9. Noble gas measurements on firn air in the Siple Dome lock-in zone, compared with $\delta O_2/N_2$. All data are gravitationally corrected and O_2/N_2 is corrected for anthropogenic effects. Ar/N_2 shows a highly systematic relationship to $\delta O_2/N_2$, as expected from prior studies on trapped air in bubbles [5,6,18]. This close relation suggests that both Ar and O_2 are excluded during the bubble close-off process, in a ratio of 0.33:1 (slope = 0.33 ± 0.02, 95% confidence interval). In contrast, note the absence of a trend in Kr/N_2 and Xe/N_2, which suggests that Kr and Xe are retained in the bubbles in proportion to N_2 (Kr slope = +0.024 ± 0.038, 95% confidence interval; Xe slope = +0.038 ± 0.08, 95% confidence interval).

handling and storage [18]. It is possible that Ar permeability in ice is a stronger function of temperature than that of O_2, so that at warm temperatures Ar loss increases relative to O_2. Observations of Ar permeability will help resolve this question.

As observed at South Pole, Kr and Xe do not show a trend in the Siple Dome lock-in zone (Fig. 9). This supports the inference made from South Pole data, that a threshold molecular diameter of ~3.6 Å exists, above which gases are not affected by the close-off fractionation. This fact is especially significant given that firn structure at South Pole is very different from that at Siple Dome, where abundant hoar layers and strong metamorphism exist [36]. The absence of close-off fractionation in Kr and Xe raises hopes that past atmospheric Kr and Xe abundances might be reconstructed from ice cores. These abundances are expected to change with average ocean temperature, due to solubility effects [38,39].

5. Mass-dependent artifact

In the lock-in zone, ratios of heavy to light isotope abundances actually decrease with depth (Figs. 2 and 7). Because isotopes have identical molecular sizes, the observed trends cannot be due to size-dependent fractionation. Rather, they must reflect mass-dependent processes. In the following discussion, we show that lock-in isotope fractionation scales with mass much like gravitational enrichment. This is important because it provides justification for our practice of using measured $\delta^{40}Ar \times \Delta m$ and $\delta^{15}N \times \Delta m$ to correct the elemental ratios for all modes of mass-dependent fractionation within the lock-in zone.

Within the South Pole lock-in zone, $\delta^{40}Ar$ plotted vs. $\delta^{15}N$ shows a slope of 4 (Fig. 10), suggesting a mass-dependent fractionation process like gravitation. However, since these samples were drawn from the lock-in zone, in which vertical transport is absent, the fractionation cannot be due to gravitation. Instead, the fractionation may be a collection artifact due to pressure gradients in the firn or borehole during sampling. This artifact would arise from the strong vacuum created by the pump when sampling in the deep firn where permeability is very low. Pressure gradients are expected to fractionate gases according to Δm [40]; gravitational fractionation is a special case of pressure-gradient fractionation where the pressure gradient is imposed by hydrostatic balance.

To see that pressure-gradient fractionation produces an effect roughly consistent with our observations, consider the following. Keeling et al. [40] show that, if diffusion is the only gas transport mechanism, the observed $\delta^{15}N$ fractionation in the deepest sample, −0.06‰, could be produced by a 0.17% fractional

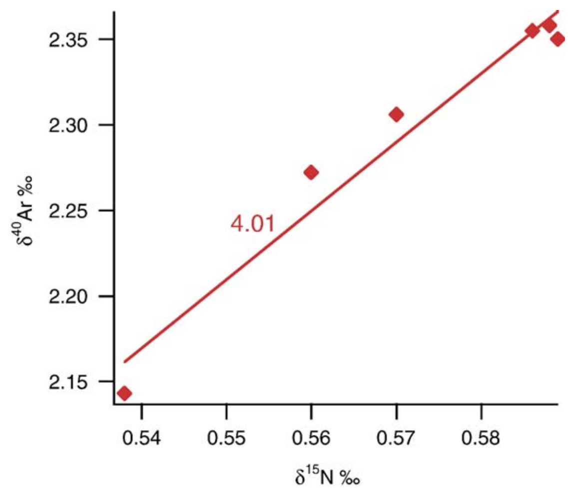

Fig. 10. $\delta^{40}Ar$ plotted vs. $\delta^{15}N$ from the South Pole lock-in zone. Because isotopes have identical molecular sizes, the isotope fractionation cannot be due to size-dependent fractionation. The slope of 4.01 suggests a mass-dependent fractionation process, like gravitational enrichment, which scales as the mass difference Δm.

pressure gradient (120 Pa pressure difference at South Pole pressures). We do not know the exact location of this gradient, but it could be in the sample intake at the bottom of the firn air sampling device. When sampling the firn, both diffusive and advective flow occur. Thus, the same fractionation could result if the pressure gradient were 100 times larger (0.12 bar) and the turbulent mixing or advective replacement time of the sampling volume were 1/100th of the relevant diffusion time. The appropriate length scales of the firn air sampling device are of order 10 cm and the diffusivity of N_2 is about 0.2 $cm^2\ s^{-1}$, so the diffusion time is of order 500 s. With a flow of 10 l min^{-1}, the advective replacement time of the ~1-l volume at the base of the device is ~6 s, making this explanation seem plausible.

Further support for this hypothesis may be provided by the Kr/N_2 and Xe/N_2 data (Fig. 11). With mass differences of 56 and 104, respectively, these gas pairs may differentiate between pressure-gradient fractionation and other known types of fractionation such as Knudsen diffusion, ordinary molecular diffusion and thermal diffusion, as illustrated in Fig. 12. In a plot of $\delta Xe/N_2$ vs. $\delta^{40}Ar$ in the lock-in zone, the observed slope of 27.5 is close to the value of 26 expected for pressure-gradient fractionation at diffusive equilibrium. Likewise, in the plot of $\delta Kr/N_2$ vs. $\delta^{40}Ar$, the observed slope of 13.6 is very close to the expected value of 14 for pressure-gradient fractionation (Fig. 12). However, this agreement may be fortuitous, as it is expected that diffusivity differences between the heavy noble gases and N_2 should also cause fractionation. Because the air is probably far from diffusive equilibrium, the data may reflect a combination of fractionation by ordinary molecular diffusion and some other process (R. Keeling, personal communication).

Another relevant observation is that sampling flow rates typically decreased markedly with depth in the lock-in zone, which we attribute to the decreasing permeability of the firn with depth in this region of transition between firn and ice. At these lower flow rates, the artifactual fractionation should increase due to less turbulent mixing and reduced advective replacement [40]. In addition, pressure gradients increase as permeability decreases, further increasing the pressure-gradient fractionation. This could explain why the fractionation effect appears to grow stronger with depth. An exception is the deepest sample at Siple

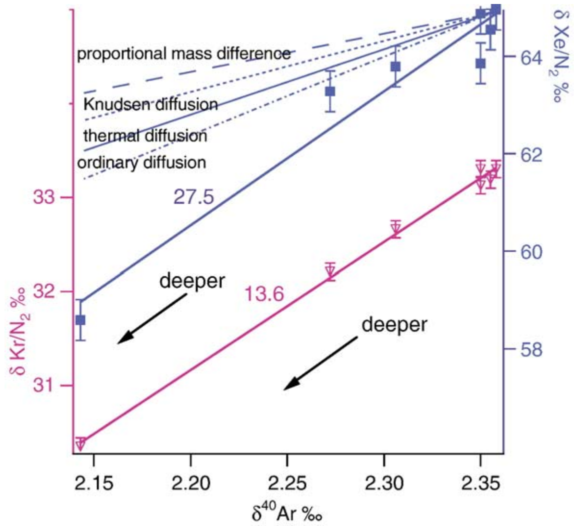

Fig. 12. $\delta Kr/N_2$ and $\delta Xe/N_2$ in the South Pole lock-in zone plotted vs. $\delta^{40}Ar$. Only data from > 116 m are shown. The observed slopes of 13.6 and 27.5 are close to the expected values for equilibrium pressure-gradient fractionation of $\Delta m/\Delta m = 56/4 = 14$ and $104/4 = 26$, for Kr/N_2 and Xe/N_2 respectively. Other fractionation processes scale as the square root of the mass ratio (Knudsen diffusion) or roughly as the proportional mass difference $\Delta m/m$ (ordinary diffusion; thermal diffusion). Because sampling conditions are far from diffusive equilibrium, some contribution to fractionation from ordinary diffusion is probable.

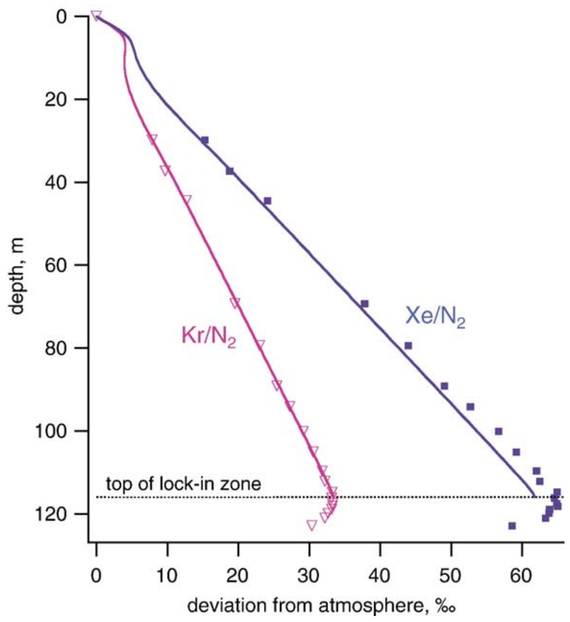

Fig. 11. $\delta Kr/N_2$ and $\delta Xe/N_2$ profiles at South Pole. These curves largely reflect gravitational enrichment, as expected. The good fit of the Kr data to the model is encouraging and supports the view that gravitational enrichment is the only significant process affecting Kr/N_2 in the open firn. The lock-in portions appear to be fractionated by some process other than gravity, however. A sampling artifact is implicated (see Section 5). The slight excess of Xe in the open firn relative to the model is not understood; we speculate that this is due to formation of a $Xe–H_2O$ complex, which has greater mass and therefore gravitational fractionation.

Dome (Fig. 9). In this particular case, flow rates returned to near-normal values, presumably because of a high-permeability layer. This sample had higher $\delta^{15}N$ and thus appears to have experienced less fractionation than the samples immediately above it. This apparent anticorrelation of fractionation with flow rate adds further support to the hypothesis of an artifactual pressure-gradient fractionation.

Tests were performed to check for possible artifactual fractionation of the gas during sampling, involving filling flasks at half and doubled flow rates from the same depth. The logic behind these tests was that, if there were fractionation occurring due to pressure gradients in the firn imposed by the pumping, it should be flow-rate sensitive because pressure gradients vary with flow rate. No effect was seen. In retrospect, the logic was flawed, because higher flow rates could translate into greater turbulent mixing and advective replacement, which counteract the fractionating effects of greater pressure gradients [40]. As we argue above, fractionation probably did occur, but would have been constant for a given firn permeability regardless of pumping rate, and so could not have been detected by this test.

In summary, our correction for gravitational fractionation using observed $\delta^{40}Ar \times \Delta m$ and $\delta^{15}N \times \Delta m$ probably also successfully corrects for the effects of an artifactual pressure-gradient and diffusivity fractionation in the lock-in zone. The amount of artifactual fractionation appears to be unimportant, because it mimics the gravitational effect and is therefore nullified whatever its size. This does, however, suggest that model-data comparisons should be done with “gravitationally” corrected data and a gravity-free model rather than raw data compared to a model including only true gravitational fractionation.

6. Discussion

The data presented here suggests that close-off fractionation increases very non-linearly with decreasing molecular size, which may shed light on the mechanism of the close-off fractionation. Neon, with a diameter of 2.82 Å, is 0.78 Å smaller than the apparent threshold value of 3.6 Å (Table 1). For O_2, this difference is a factor of 5.8 smaller. Thus, it might be reasonable to expect that Ne would be 5.8 times more fractionated than O_2. In fact, Ne is 34 ± 2 times as fractionated as O_2, roughly the square of 5.8.

Helium passes readily through the ice lattice; for this reason, helium studies on ice cores must sample the ice and place it in sealed evacuated chambers within 30 min of deep ice core retrieval to surface pressures [41]. A study of diffusion coefficients of gases in polycrystalline (i.e., natural) ice found that neon has a diffusivity (10^{-10} $m^2\ s^{-1}$) only one order of magnitude smaller than that of helium (10^{-9} $m^2\ s^{-1}$) [42]. This study also found a strong dependence of diffusivity on molecular size, with argon having a diffusivity of 10^{-11} $m^2\ s^{-1}$. Our measurements of neon in ice core samples have shown highly depleted $\delta Ne/N_2$ values, in the range of −200‰ to −600‰, suggesting that neon has leaked out of the ice core samples during several years of storage in our freezer at −25 °C. Ar/N_2 values in ice that has been stored for many years are also somewhat depleted, typically −5‰ to −10‰.

The hypothesis advanced recently by Ikeda-Fukazawa et al. [21] and adopted by our present work is that Ne, O_2, Ar and N_2 diffusion occurs through the ice lattice itself. Based on molecular dynamics simulations, the mechanism of diffusion for all but the small molecules Ne and He may involving breaking of hydrogen bonds [43]. An entirely different mechanism, the “interstitial mechanism”, dominates the transport of Ne and He [43]. It is possible that data similar to those reported here, from sites at differing temperatures, could be used to distinguish the two mechanisms, if their temperature dependences are divergent.

Recently, Huber et al. [44] have proposed that fractionation of He, Ne, Ar and O_2 during bubble close-off occurs because the ice lattice itself has a “hole” with a diameter of ~3.6 Å, through which these gases can escape. From firn air data similar to ours, they infer the existence of a critical size, 3.6 Å, below which gases are fractionated. They show that the ice lattice geometry produces a regular structure with a gap of ~3.6 Å.

Bender et al. [18] explained losses of O_2 and Ar in storage or handling of ice samples by proposing that “configurational diffusion” of gases in microcracks or very small openings could provide the observed size dependence of the fractionation, as described by Kärger and Ruthven [45]. This mechanism may also cause the close-off fractionation. Our data may be useful for testing these hypotheses, because some mechanisms do not predict a threshold size. For example, mechanisms that are mass-dependent, such as Knudsen diffusion and ordinary molecular diffusion, are clearly ruled out by our finding of a lack of fractionation in molecules larger than 3.6 Å even with large mass differences (e.g., Kr/N_2 and Xe/N_2).

7. Implications for ice core and firn air studies

The inferred flux of Ne, O_2 and Ar to the atmosphere in the firn at our two sites implies that the bubbles in mature ice (i.e., with the bubbles fully closed) should be depleted in these gases relative to N_2 due to the close-off fractionation. Observations of O_2 and Ar in ice do indeed show depletions and are generally consistent with this expectation, although the depletions also reflect artifactual gas loss during core storage and handling [18]. A corollary is that low-density layers in ice should contain more O_2 and Ar than high-density layers, because the low-density layers are expected to have closed off later and thus accumulated excluded O_2 and Ar in a lock-in zone. In other words, gas ratios should vary with an annual cycle in cores where annual layers are resolved. These cycles arise not from seasonal changes in atmospheric gas composition, but from density differences in the firn at the time of close-off [46]. At most sites, the low-density layers are summer layers and the high-density layers are winter layers. A practical application of this idea is that reproducibility of ice core gas analyses can be improved by cutting the ice longitudinally in the core, so each sample averages over several annual layers [17].

A logical extension of this work would be to see if the relationship between O_2/N_2 and local summer insolation found in the Vostok and Dome Fuji ice cores [19,20] also applies to Ne/N_2. We would predict, based on our observations, that Ne/N_2 covariation with local insolation should be found with an amplitude 34 times larger than that of O_2/N_2. This work could help improve astronomical dating of ice cores and help shed light on the mechanism by which O_2/N_2 records local insolation. Sampling for Ne/N_2 may be difficult as samples probably need to be taken in the field, shortly after core retrieval, to avoid leakage of Ne out of the ice cores. Another possible complication of Ne measurements in ice arises from the high solubility of Ne in the ice lattice [47], which may lead to higher-than-atmospheric Ne/N_2 ratios in melt extractions from the bulk ice.

Similarly, studies that use ice core Kr/Ar [38] or Ar/N_2 must account for the close-off fractionation. Ice core Kr/Ar is consistently higher than expected from gravitational enrichment alone by 4–6‰ [11], probably due to loss of Ar during the close-off fractionation.

Firn air studies of atmospheric H_2, which has a molecular size similar to Ne, will probably be biased by the close-off fractionation, especially in the lock-in zone where the oldest air is obtained. Based on the comparison with Ne, H_2 mixing ratios can be expected to be up to 10% enriched by the close-off fractionation in the oldest air. It is not known what the effect on H_2 isotopes might be. Ne isotope studies of firn air would illuminate this issue.

Firn air studies of O_2/N_2 may allow us to reconstruct atmospheric O_2/N_2 over the past century, if corrections can be made for the close-off fractionation using measured Ne/N_2 and Ar/N_2. A record of atmospheric O_2/N_2 would place much-needed constraints on past carbon cycling, as O_2/N_2 is sensitive to fewer processes than CO_2 (mainly fossil fuel combustion and terrestrial biospheric exchange [2,48,49]). Our firn air data are broadly consistent with the −0.7‰ decline in atmospheric O_2/N_2 since 1910 AD inferred from fossil fuel burning records (see Appendix A). Much more work is needed to realize this approach, however. Several more firn air studies with Ne measurements are needed to assess the stability of the ratio of fractionation under varying conditions (temperature, accumulation rate and degree of snow metamorphism). An even more ambitious goal is the reconstruction of atmospheric O_2/N_2 histories over the 10^6-yr time scale covered by ice cores. This would require that the close-off fractionation be thoroughly understood and corrected for, using the large and growing suite of measured inert gases trapped in the ice along with the O_2.

8. Conclusions

Air sampled from the firn at two Antarctic sites shows sharp enrichments in neon, O_2 and argon at the bottom of the firn in the firn–ice transition region. We hypothesize that these observations may be explained by the fact that compression of the newly formed bubbles causes bubble air pressure to increase, resulting in partial pressure gradients of all gases across a thin wall of ice that separates the bubble from the open firn. A simple model of fractionation across this wall, combined with sealing of firn air by impermeable layers 5–10 m above the bubble close-off horizon, explains the observed firn air trends quantitatively. The fractionation causes bubbles to become depleted in neon, O_2 and argon relative to the air composition prior to bubble closure, although the model predicts about a factor of 4 less O_2 depletion than observed in ice samples (see discussion in Appendix A). A residual of fractionated air rich in these gases accumulates in the remaining open firn layers, which are cut off from mixing with the atmosphere and with each other in the “lock-in zone”. This leads to a progressive enrichment of these gases in the sealed layers with time (and depth).

The pattern of fractionation in different gases deduced from the firn air samples shows a strong inverse relationship with effective molecular diameter inferred from viscosity data, but no clear trend with molecular mass. We conclude that the close-off fractionation is primarily size-dependent, as inferred by Battle et al. [2], Severinghaus et al. [11] and Huber et al. [44]. The large atoms Kr and Xe show no significant trends in the lock-in zone, where neon and O_2 trends are prominent, suggesting that Kr and Xe are not affected by the close-off fractionation. This observation implies the existence of an effective size threshold of ~3.6 Å, above which molecules have a low probability of escape from the bubbles and therefore do not become significantly fractionated. This places constraints on proposed mechanisms for the size-dependent fractionation. Our data are consistent with the recent suggestion of Huber et al. [44] that the regular crystal structure of the ice lattice contains a hole ~3.6 Å in diameter that sharply increases the escape probability of gases smaller than this size. Our data also are consistent with the hypothesis of Ikeda-Fukazawa et al. [21], that fractionation occurs because of size-dependent differential permeation of gases through the ice lattice.

This size-dependent fractionation during bubble close-off must be taken into account by ice core studies that employ Ne, O_2 or Ar. Importantly, no evidence for close-off fractionation is seen for molecules larger than 3.6 Å. This is true for the noble gases Kr and Xe as well as the greenhouse gases CO_2, CH_4 and N_2O, confirming the integrity of the ice core archive for records of these atmospheric gases.

The strong correlations of Ne and Ar with O_2 in the lock-in zone implies that a predictable physical process causes the fractionation. Future firn air studies may exploit these correlations to reconstruct atmospheric O_2/N_2 ratios over the course of the Industrial Revolution, by correcting O_2/N_2 for the size-dependent fractionation using measured noble gases. This would add a constraint to our understanding of the human perturbation of the terrestrial carbon cycle [50,51].

The lack of natural fractionation evident in Kr/N_2 and Xe/N_2 opens the possibility that these ratios may be faithfully reconstructed in the past atmosphere from ice cores, with appropriate corrections for gravitational and thermal enrichment using $^{40}Ar/^{36}Ar$ and $^{15}N/^{14}N$. Atmospheric variations in these quantities are thought to reflect average ocean temperature changes, due to the temperature dependence of the solubility [38]. Records of atmospheric Kr/N_2 and Xe/N_2 from ice cores may therefore ultimately place constraints on the magnitude and timing of average ocean temperature variations [39].

Acknowledgments

Michael Bender contributed to the sampling at South Pole, and provided mentoring, financial support and gas analysis. The manuscript was improved by his in-depth review. Ralph Keeling and Kenji Kawamura made helpful comments. We thank Earl Ramsey and Jerome Brown of the Polar Ice Coring Office for assistance in drilling at Siple Dome, Jay Kyne and Tony Wendricks for drilling at South Pole, and Jim Butler, Andy Clarke and Jesse Bastide for assistance with sample collection. Bob Mika did the analyses at Princeton and Derek Mastroianni did the analyses at SIO. CO_2 analyses were provided by Pieter Tans. Glenn Ierley helped with the analytical model. We thank Markus Leuenberger, Christof Huber and Jakob Schwander for helpful collaboration. The manuscript benefited from reviews by two anonymous reviewers. Support for this study came from the NSF Office of Polar Programs, Antarctic Glaciology Division (OPP97-25305 and OPP02-30452 to J.P.S.; OPP02-30260 to Michael Bender) and from the Gary Comer Science and Education Foundation (gifts to J.P.S. and Michael Bender).

Appendix A. Firn air and lock-in zone model

A.1. Model overview

The model is a one-dimensional finite-element treatment of the firn layer, building on earlier work by Schwander et al. [1], Battle et al. [2], Trudinger et al. [32] and Severinghaus et al. [13]. The model consists of two distinct parts: the open firn, in which diffusion takes place, and the lock-in zone. The open firn model is closely related to the model of Severinghaus et al. [13] and includes gravitational fractionation and thermal diffusion, in addition to heat transfer, as well as a convective zone. The lock-in zone portion of the model is a nearly closed system with two compartments, bubbles and open porosity. No vertical gas diffusion occurs in the lock-in zone, and the air ages at nearly the same rate as the surrounding ice. Air is simply advected downward by one annual layer per year within the lock-in zone. A small amount of air is expelled from each layer into the overlying layer each year due to the assumption that the open pores remain at ambient pressure. Each annual layer's open porosity is assumed to be an internally well-mixed reservoir, which can compositionally evolve due to permeation fractionation during bubble close-off. The amount of air occluded in bubbles in each time interval is given by the change in closed porosity, which is a prescribed function of bulk density. The depth, density, and porosity of the firn are static and are assumed to be in steady state; only the gas composition, air content and temperature can evolve.

The bottom of the lock-in zone is defined by the point at which open porosity goes to zero. While highly simplified, this model provides a starting point to examine the phenomenon of close-off fractionation and its expression within and above the lock-in zone.

Fractionation during bubble close-off occurs in both the open firn and the lock-in zone. The model is built upon the hypothesis that fractionation is caused by differential permeation of gases through the ice lattice in response to bubble overpressure. The model supposes that a thin wall of ice separates the newly formed bubble from the open pores and permeation is dominantly through this wall. This flux of fractionated gas leaving the newly formed bubble alters the firn air composition. A complementary effect occurs on the air remaining behind in the bubble as required by mass conservation. The instantaneous flux of gas n from an ensemble of N bubbles in a cubic meter of firn is given by

$$F_n = D_n X_n x_n P/\gamma A N = J_n N \qquad \text{mol m}^{-3}\ \text{s}^{-1} \tag{A1}$$

where F_n is the flux of gas n per unit volume of bulk firn, D_n is the diffusivity of gas n in the ice lattice, X_n is the solubility of gas n in ice, x_n is the mole fraction of gas n in the bubble air, P is ambient pressure in the open pores, γ is the unknown constant relating to wall thickness, A is the unknown constant describing the effective area of the wall available for permeation and J_n is the instantaneous flux from a single bubble (Fig. 3). The number of bubbles N contributing to the flux is given by the volume of bubbles V_c with less compression than the critical compression (taken to be 0.05 or 5%) divided by the average individual bubble volume V_{bubble}:

$$N = V_c/V_{\text{bubble}} \qquad \text{m}^{-3} \tag{A2}$$

$$V_c = \sum \Delta V_{b(j)} \quad \text{for} \ \ (s_j/s-1)<0.05 \qquad \text{m}^3\ \text{m}^{-3}. \tag{A3}$$

Here $\Delta V_{b(j)}$ is the volume of newly enclosed bubbles at an overlying grid point j, s_j is the porosity at grid point j and s is the porosity at the grid point where N is being calculated. For practical reasons, V_c is computed by summing the volumes of bubbles formed at overlying grid points that meet the criteria of having less than 5% compression. The average bubble volume V_{bubble} is taken to be a constant 10^{-10} m^3, corresponding to a sphere with diameter 0.576 mm. A refinement of the model might include variable bubble size; however, we expect that the area A will also increase with bubble size. This would partially cancel the effect of increasing bubble size; for simplicity, we avoid this refinement in the present model.

On physical grounds, the permeation fractionation is not expected to be a constant, so the usual concept in geochemistry of "fractionation factor" is avoided. Instead, the model keeps track of the number of moles M_n of gas n in each reservoir and computes the air composition as follows. The air composition q is defined as the ratio of a sample gas ratio R_{SA} to a standard R_{ST}, which for inert gases is the free atmosphere (for O_2 the standard is a 70-l tank of dry air known as Glass Flask 1 or GF1, which is maintained by M. Bender at Princeton University):

$$\begin{aligned} &q \equiv R_{SA}/R_{ST} \\ &R_x = M_{Ne}/M_{N2}, M_{O2}/M_{N2}, M_{Kr}/M_{N2}, \text{etc.} \end{aligned} \tag{A4}$$

The air composition q is related to the familiar delta notation in per mil units by:

$$\delta = [q-1]10^3‰, \ q = (\delta/10^3 + 1). \tag{A5}$$

In concept, a small volume increment of air ΔV is occluded in bubbles in a given time step, starting from an initial open volume V, leaving the remaining open volume V':

$$V' = V - \Delta V \qquad \text{m}^3\ \text{m}^{-3}. \tag{A6}$$

In practice, the volume V is taken to be the open porosity s_o and the increment ΔV the increment Δs_o. The increment Δs_o is calculated from the change in s_o from one grid cell to the next in the numerical discretization, and is corrected for bubble compression. We model Δs_o in the following way.

The open firn model has a grid size of 0.5 m and the lock-in model has a variable grid size equivalent to 1 yr of snow accumulation. The lock-in depth (LID) is specified and calculation of the lock-in grid depths begins at the LID in the model initialization. Lock-in zone grid depths are found by integrating the density vs. depth curve and dividing by mass accumulation rate to obtain ages, with the assumption that the grid point lies in midsummer. This is intended to simulate the observation that the winter layers are higher-density and provide the sealing layer, trapping air in the summer layer below. The first lock-in grid point corresponds to the first midsummer that the model encounters below the LID. A very small depth increment is used in the initialization (5e−7 m) to insure that the grid spacing varies smoothly.

The model then calculates bulk density ρ at each grid point using the curves fitted to the density data (Figs. A1 and A2), with the coefficients given in Table A1. Temperature is from observed temperature profiles [13]. Next, the total porosity s is calculated via:

$$s = 1 - \rho/\rho_{ice} \qquad m^3\ m^{-3} \tag{A7}$$

$$\rho_{ice} = 916.5 - 0.14438 T_K - 0.00015175 T_K^2 \qquad kg\ m^{-3} \tag{A8}$$

[52]

A.2. Closed porosity parameterization

The most critical and subjective choice in the model is the choice of a closed porosity s_c parameterization. We found we were able to produce an acceptable match to the firn air data using a least-squares fit to measured closed porosity data [1]. A two-part curve was found (Fig. A3), with the linear portion obtained by geometric mean regression of the data between 811.6 and 850 kg m^{-3}, and the exponential portion forced by eye to join the linear portion smoothly. The resulting closed porosity used in the model is:

$$s_c = s \exp[75(\rho/837.3 - 1)] \qquad \rho < 815\ kg\ m^{-3}$$
$$s_c = 0.0016105\rho - 1.297 \qquad \rho \geq 815\ kg\ m^{-3}$$
$$s_c = s \qquad s_c > s. \tag{A9}$$

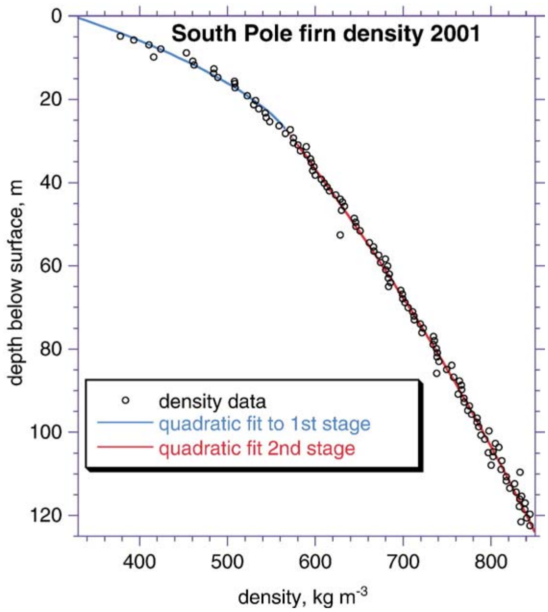

Fig. A1. Firn bulk density vs. depth from firn core measurements taken in association with the 2001 South Pole firn air experiment (Hole 1). Measurements were made during drilling by measuring the core piece dimensions to compute bulk volume and weighing. Density used in the model is the quadratic fit shown.

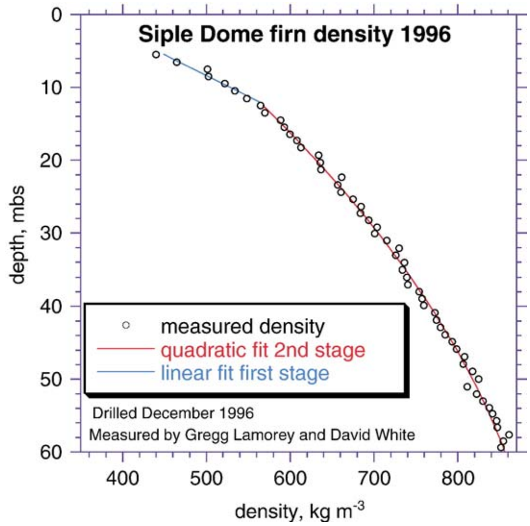

Fig. A2. Siple Dome firn bulk density vs. depth from firn core measurements taken in association with the 1996 firn air experiment (the "C core"). Measurements were made during drilling by measuring the core piece dimensions to compute bulk volume and weighing. Density used in the model is the combined quadratic and linear fit shown.

We caution that the slope of the linear portion may not be steep enough, due to the possibility that the closed porosity data suffered from cut-bubble effects (J. Schwander, personal communication). As the length scale is found by fitting to the data, a steeper slope would simply force the length scale to be smaller; in essence, only the product of the slope and the length scale has a strong constraint placed upon it by the firn air data. Thus, the value of the length scale by itself may have little physical significance.

The open porosity is calculated from:

$$s_o = s - s_c \qquad m^3\ m^{-3} \tag{A10}$$

A.3. Correction for bubble compression

Because of the assumption of steady state, we may use the change in closed porosity Δs_c from one grid point to the next below as a proxy for the change over time in s_c undergone by a given mass of firn. The time interval during which this change occurs is equal to the transit time τ required for a particle of firn to move from one grid point to the next. However, Δs_c is a biased estimate of the amount of air enclosed in bubbles, for three distinct reasons. First, the existing bubble population's volume is shrinking through compaction during this time interval. Second, newly formed bubbles also shrink, such that approximately half of the newly formed volume has been subjected to compaction by the end of the time interval. Third, the amount of trapped air is expressed per unit volume, not per unit mass, so part of Δs_c is due to the increase in density rather than creation of new bubbles, so a correction for the increase in density is needed.

Our correction for these compression effects follows the assumption that the bubble volumes change in proportion to the change in total porosity s. Because the bubble pressures are very small compared to the load [29], the compression of bubbles should not be retarded substantially by the internal pressure at this stage of the densification process.

Following this logic, if no new bubbles were added to the population between grid point $(i-1)$ and grid point (i), the closed volume would shrink by a factor $s_{(i)}/s_{(i-1)}$. The observed change in closed porosity Δs_c therefore may be written as the sum of the true increment of volume added in new bubbles ΔV_b between grid point $(i-1)$ and grid point (i), the two bubble compression terms and the density correction:

$$\Delta s_c = \Delta V_{b(i)} - [s_{c(i-1)} - s_{c(i-1)} s_{(i)}/s_{(i-1)}] - [0.5\Delta V_{b(i)} - 0.5\Delta V_{b(i)} s_{(i)}/s_{(i-1)}] + [s_{c(i-1)} \rho_{(i)}/\rho_{(i-1)} - s_{c(i-1)}]$$

$$\Delta s_c \equiv s_{c(i)} - s_{c(i-1)} \quad \text{(A11)}$$

rearranging to solve for $\Delta V_{b(i)}$

$$\Delta V_{b(i)} = 2\{s_{c(i)} - s_{c(i-1)}[s_{(i)}/s_{(i-1)} + \rho_{(i)}/\rho_{(i-1)} - 1]\} / [s_{(i)}/s_{(i-1)} + 1] \quad \text{m}^3\ \text{m}^{-3}. \quad \text{(A12)}$$

The total trapped air at each grid point is tracked, with a second density correction, as

$$V_{b(i)} = V_{b(i-1)} \rho_{(i)}/\rho_{(i-1)} + \Delta V_{b(i)} \quad \text{m}^3\ \text{m}^{-3} \quad \text{(A13)}$$

$$V_{b(i)} \neq s_{c(i)} \quad \text{(A14)}$$

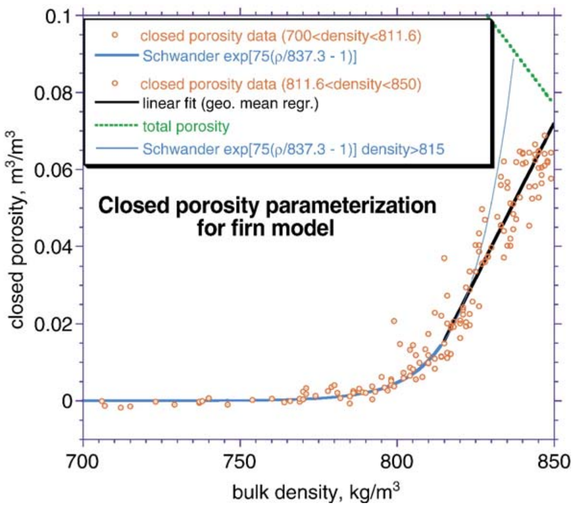

Fig. A3. Basis for the closed porosity parameterization used in the model. The data are measured closed porosity from Summit, Greenland [1]. Curve fit was made by subjectively choosing 811.6 and 850 kg m^{-3} to represent the bounds of the "linear" portion of the curve. These data in this interval were then fit by geometric mean regression. Next, the Schwander [7] closed porosity parameterization was adjusted to give a good fit by eye to the data between 700 and 811.6 kg m^{-3}, with the added constraint that the curves meet smoothly (see Appendix A.2).

Table A1
Site-specific input parameters used in the model

	South Pole	Siple Dome	Units
Density curve fit coefficients			
Critical depth	27	12	m
a	324.47	352.98	kg m^{-3}
b	13.748	17.524	kg m^{-3} m^{-1}
c	−0.17786	0	kg m^{-3} m^{-2}
$\rho = a + bz + cz^2$ (depth < critical depth)			
d	464.3	447.69	kg m^{-3}
e	3.9348	10.339	kg m^{-3} m^{-1}
f	−0.0066525	−0.058786	kg m^{-3} m^{-2}
$\rho = d + ez + fz^2$ (depth ≥ critical depth)			
Other parameters			
Annual average temperature	−51.0	−25.4	°C
Geothermal gradient	0.0027	0.01	°C m^{-1}
Ice accumulation rate	0.080	0.111	m yr^{-1}
Mass accumulation rate	73.9	102	kg m^{-2} yr^{-1}
Run duration	201	196	yr
Barometric pressure	68,100	93,700	Pa
Convective zone:			
Surface eddy diffusivity	3.0×10^{-5}	3.0×10^{-5}	m^2 s^{-1}
Eddy diffusivity scale depth	2.0	1.0	m
Lock-in depth	116	49	m
Grid spacing in open firn	0.5	0.5	m
Grid spacing in lock-in zone	1	1	yr

It must be emphasized that the V_b term has the same units as porosity ($m^3\ m^{-3}$). It may be thought of as the integral of the volumes of all the bubbles at the time they closed off. It corresponds to the volume of trapped air corrected to ambient barometric pressure P (Pa) and is used to calculate the model's total air content:

$$\text{Total air content} = (V_{b(i)} + s_{o(i)})P/101325 \times 273.15 / T_K/\rho_{(i)} 10^6 \quad \text{ml}_{STP}\ \text{kg}^{-1} \quad (A15)$$

A.4. Time-dependent evolution of the lock-in zone

Within the lock-in zone, gas compositions in the bubbles and the open (summer) part of each annual layer are computed once per year, while transferring the value down one layer to simulate the downward advection due to snow accumulation. The total moles of air M_{air} per cubic meter in bubbles, open firn pores and the increment of new bubbles are calculated from the ideal gas law:

$$M_{air(bubble)(i-1)} = PV_{b(i-1)}/(RT_K) \quad \text{mol m}^{-3} \quad (A16)$$

$$M_{air(firn)(i-1)} = Ps_{o(i-1)}/(RT_K) \quad \text{mol m}^{-3} \quad (A17)$$

$$M_{air(added)(i)} = P\Delta V_{b(i)}/(RT_K) \quad \text{mol m}^{-3} \quad (A18)$$

Mole fractions are calculated according to the approximation:

$$x_{N2} + x_{O2} + x_{Ar...} \approx 1 \quad \text{mol mol}^{-1} \quad (A19)$$

where $x_{Ar...}$ includes all trace gases in dry air and is taken to be a constant 0.00974. Because O_2 is a major gas in air, its variations have a significant impact on the mole fractions of other gases by dilution. Dilution is accounted for by considering, from (A4):

$$q_{O2} \equiv (x_{O2}/x_{N2})/(x_{O2(ST)}/x_{N2(ST)}) \quad \text{unitless} \quad (A20)$$

where $x_{n(ST)}$ denotes the standard mole fraction (0.20946 for O_2 and 0.7808 for N_2). Combining (A19) and (A20):

$$x_{N2} = [1 - x_{Ar...}]/[1 + q_{O2}x_{O2(ST)}/x_{N2(ST)}] \quad \text{mol mol}^{-1}. \quad (A21)$$

In the case where O_2 is not modeled, because another gas n is being modeled, the value of q_{O2} for the purpose of the dilution correction is approximated by $[(q_n - 1)/R_{oe} + 1]$, where R_{oe} is the empirical ratio of enrichment of gas n to O_2 obtained from plots such as Fig. 6 ($R_{oe}=34$ for neon and 1 for O_2, for example):

$$x_{N2} \approx [1 - x_{Ar...}]/[1 + \{(q_n - 1)/R_{oe} + 1\} x_{O2(ST)}/x_{N2(ST)}] \ \text{mol mol}^{-1}. \quad (A22)$$

The mole fraction of any gas n (other than N_2) is found from the definition of q, Eq. (A20):

$$x_n = x_{n(ST)} q_n x_{N2}/x_{N2(ST)} \quad \text{mol mol}^{-1} \quad (A23)$$

where

$$q_n \equiv (M_n/M_{N2})/(x_{n(ST)}/x_{N2(ST)}) \quad \text{unitless.} \quad (A24)$$

The inventory in moles M_n of gas n in a given reservoir is found from:

$$M_{n(bubble)} = x_n M_{air(bubble)},\ M_{n(firn)} = x_n M_{air(firn)},\ \text{etc.} \quad \text{mol m}^{-3}. \quad (A25)$$

Each year, the new inventory $M'_{n(i)}$ of gas in the bubbles at grid point i is computed from the inventory in the overlying layer (grid point $i-1$), and the time-integrated fluxes from permeation and new bubble closure:

$$M'_{n(bubble)(i)} = M_{n(bubble)(i-1)} - F_{n(i)}t_a + M_{n(added)(i)} \quad \text{mol m}^{-3} \quad (A26)$$

where t_a is the number of seconds per year.

Computation of the inventories in the open pores of the lock-in zone is slightly more complicated, because some gas must be expelled from open pores (summer layers) into overlying layers and into the open firn column as the firn compacts. This expulsion of air from locked-in layers is required by conservation of mass and our assumption that the pressure in the open pores remains at ambient. That this expulsion occurs in Nature is supported by observations of total air content in Greenland ice, which suggest that pressure starts to build, and leakage stops, at a bulk density ρ_{co} about 14 kg m^{-3} greater than the typical lock-in density [9]. This observation can be explained by considering the three-dimensional nature of firn. Even a highly layered firn typically has sastrugi or other irregularities in a given layer every few meters [36]. Air can travel horizontally over several meters to leaks in a sealing layer that permit the air to escape to a layer above by viscous flow. The tortuosity of such a path is, however, much too high to permit significant vertical diffusion. Thus, air can escape from the lock-in zone without bidirectional flow and vertical diffusive mixing. We recognize that our assumption of ambient pressure in open pores is an extreme and that in reality some overpressure of open pores probably occurs in the lower part of the lock-in zone. However, we do not know how to model this at present and so adopt the simplification of ambient pressure in open pores. The fact that the model produces ice with realistic air contents (Appendix A.8) suggests that this assumption is not badly wrong.

The amount of air expelled E_{air} from each layer each year is calculated from the change in vertically integrated open pore inventory, which depends on the layer thickness z_{layer}. Note the change in units (mol m^{-2}) from other volume terms in the model. The permeation flux F_{air} is approximated from the sum of O_2 and N_2 fluxes with a factor for Ar and trace gases:

$$E_{air(i)} = (M_{air(firn)(i-1)} - M_{air(bubble)(i)})z_{layer(i-1)} - (M_{air(firn)(i)} - F_{air(i)}t_a)z_{layer(i)} \quad \text{mol m}^{-2} \quad \text{(A27)}$$

$$F_{air(i)} \approx [F_{O2(i)} + F_{N2(i)} \times (1 + x_{Ar...}/x_{N2(ST)})] \quad \text{mol m}^{-3}\ \text{s}^{-1}. \quad \text{(A28)}$$

All expelled air is assumed to flow upwards, finally exiting the lock-in zone at the lock-in horizon. The total flux of air into a given layer is therefore the cumulative sum of expelled air $\sum E_{air(i)}$ from all lower layers. Expelled air is assumed to mix completely with the air in an overlying layer. Therefore, the composition of the flux may be taken to be the composition of the upstream layer (with respect to layer (i−1) this is layer (i)). The mole fractions of N_2 and gas n entering a layer are calculated from Eqs. (A22) and (A23), and the total gas fluxes are:

$$E_{N2(i)} = x_{N2(i)}\Sigma E_{air(i)} \quad \text{mol m}^{-2} \quad \text{(A29)}$$

$$E_{n(i)} = x_{n(i)}\Sigma E_{air(i)} \quad \text{mol m}^{-2}. \quad \text{(A30)}$$

The new inventory $M'_{n(i)}$ of gas in the open pores at grid point i may now be calculated from the divergence of the expulsion flux, the permeation term and the new bubble term:

$$M'_{N2(firn)(i)} = M_{N2(firn)(i-1)} + (E_{N2(i)} - E_{N2(i-1)})/z_{layer(i)} + F_{N2(i)}t_a - M_{N2(added)(i)} \quad \text{mol m}^{-3} \quad \text{(A31)}$$

$$M'_{n(firn)(i)} = M_{n(firn)(i-1)} + (E_{n(i)} - E_{n(i-1)})/z_{layer(i)} + F_{n(i)}t_a - M_{n(added)(i)} \quad \text{mol m}^{-3}. \quad \text{(A32)}$$

New gas compositions for bubbles and open pores are finally calculated from:

$$q'_n \equiv (M'_n/M'_{N2})/(x_{n(ST)}/x_{N2(ST)}) \quad \text{unitless} \quad \text{(A33)}$$

A.5. Time-dependent evolution of the open firn

Within the open firn, computation of the effect of bubble close-off fractionation on the remaining gas composition is more complex than in the lock-in zone. The grid size is large compared to the distance traveled by the firn in one time step (~$10^5\times$), yet the volume of bubbles formed is calculated from the change across one entire grid cell. We make the approximation that the volume enclosed in bubbles in each time step depends on the ratio of the time step Δt to the transit time τ, which in turn depends on the grid size Δz, the ice accumulation rate $\dot{b}$ and the ratio of density to ice density.

$$\tau_{(i)} = \Delta z/\dot{b}\rho_{(i)}/\rho_{ice} \quad \text{s} \quad \text{(A34)}$$

For example, at South Pole τ is about 5 yr near the lock-in horizon, compared to a typical value of Δt=1/20,000 yr (for a grid size of 0.5 m).

Computation of the inventories is done in a similar fashion as in the lock-in zone, except for the added air term:

$$M_{air(bubble)(i)} = PV_{b(i)}/(RT_K) \quad \text{mol m}^{-3} \quad \text{(A35)}$$

$$M_{air(firm)(i)} = PS_{o(i)}/(RT_K) \quad \text{mol m}^{-3} \quad \text{(A36)}$$

$$M_{air(added)(i)} \approx P\Delta V_{b(i)}\Delta t/\tau_{(i)}/(RT_K) \quad \text{mol m}^{-3}. \quad \text{(A37)}$$

Mole fractions are found as in Eqs. (A22) and (A23), and the new inventories (excepting firn gas transport model fluxes, see Eq. (A45)) are found by:

$$M'_{N2(firn)(i)} = M_{N2(firn)(i)} + F_{N2(i)}\Delta t - M_{N2(added)(i)} \quad \text{mol m}^{-3} \quad \text{(A38)}$$

$$M'_{n(firn)(i)} = M_{n(firn)(i)} + F_{n(i)}\Delta t - M_{n(added)(i)} \quad \text{mol m}^{-3}. \quad \text{(A39)}$$

The average gas composition of bubbles is also tracked in time. This calculation must take into account the downward advection J_b of gas in bubbles, which depends on the vertical velocity and concentration gradient. The flux $J_{b(out)}$ leaving a given grid cell (i) is computed from the vertical velocity $\dot{b}\,\rho_{ice}/\rho$, gas composition q and bubble volume V_b averaged between grid point (i) and (i+1). This linear approximation is adequate considering the very small fluxes and is a common numerical technique [53]. Mole fractions $x_{n(i+0.5)}$ are computed from averaged q as in Eqs. (A22) and (A23). For brevity, fluxes of N_2 are not written separately here.

$$J_{bn(out)(i)} \approx \dot{b}\rho_{ice}[1/\rho_{(i)} + 1/\rho_{(i+1)}]/2x_{n(i+0.5)}P10^2/(RT_K)[V_{b(i)} + V_{b(i+1)}]/2 \quad \text{mol m}^{-2}\text{ s}^{-1} \tag{A40}$$

By continuity, the flux $J_{b(in)}$ entering grid cell (i+1) must equal the flux exiting cell (i):

$$J_{bn(in)(i+1)} = J_{bn(out)(i)} \qquad \text{mol m}^{-2}\text{ s}^{-1} \tag{A41}$$

$$\Delta J_{bn(i)} = J_{bn(in)(i)} - J_{bn(out)(i)} \qquad \text{mol m}^{-2}\text{ s}^{-1} \tag{A42}$$

New bubble inventories are calculated from:

$$M'_{n(bubble)(i)} = M_{n(bubble)(i)} - F_{n(i)}\Delta t + M_{n(added)(i)} + \Delta J_{nb}\Delta t/\Delta z \quad \text{mol m}^{-3}. \tag{A43}$$

The new gas compositions in bubbles and open firn are found from:

$$q'_n = (M'_n/M'_{N2})/(x_{n(ST)}/x_{N2(ST)}) \qquad \text{unitless.} \tag{A44}$$

This close-off fractionation model is embedded within a firn gas transport model. For simplicity, the firn gas transport model does not treat gases independently from $^{28}N_2$, as done in the close-off fractionation model. Instead, it treats the ratio of a gas to $^{28}N_2$, expressed as $\delta \equiv [q-1]\cdot 10^3$‰.

A.6. Firn gas transport model (the "old model")

The governing equation of the gas component of the basic firn air model without close-off fractionation is (see Table A2 for a full list of symbol meanings):

$$s_o\frac{\partial\delta}{\partial t} = \frac{\partial}{\partial z}\left[s_o D_{mol}(z,T,p)\left(\frac{\partial\delta}{\partial z} - \frac{\Delta mg}{RT_K} + \Omega\frac{\partial T}{\partial z}\right)\right] + \frac{\partial}{\partial z}\left[s_o D_{eddy}(z)\frac{\partial\delta}{\partial z}\right]. \tag{A45}$$

This model is identical to that of Severinghaus et al. [13], with the exception of an added term for open porosity s_o, which was neglected by [13]. The gradient of open porosity is important in transient simulations because s_o occurs inside the derivative in Eq. (A45). Also, the right-hand term on the right-hand side of Eq. (A45) was not shown in [13], although it was used and described. This term simulates the convective zone with an eddy diffusivity D_{eddy} that decays exponentially with depth. The exponential form is expected based on theoretical models of windpumping in polar firn [30]. The surface magnitude and the scale depth of the eddy diffusivity are arbitrary, however, and are fit to data (Table A1).

The profile of effective molecular diffusivity D_{mol} in the open part of the firn is found by tuning to match observed CO_2 concentrations in firn air (Figs. A4 and A5), following a standard technique used by other workers [2,31,32]. The upper boundary condition used in the model is the independently known atmospheric CO_2 concentration history (Fig. A6). This process also identifies the lock-in depth, as the point at which the deduced diffusivity goes to zero.

The model is discretized on a grid with spacing Δz of 0.5 m, the same grid used for the close-off fractionation model. Diffusivities and other gas-specific transport parameters [54,55] are shown in Table A3. Fluxes are computed using the values of open porosity s_o and effective diffusivity D_{mol} halfway between the grid points, which is a common approximation [53]. The flux j_{in} to a given grid point (i) thus uses the porosity and effective diffusivity at the depth corresponding to (i−0.5), and the flux j_{out} away from the grid point uses a different open porosity and effective diffusivity, at the depth corresponding to (i+0.5):

$$j_{in} = -s_{o(i-0.5)}D_{mol(i-0.5)} \times \frac{\left[\delta_{(i)} - \delta_{(i-1)} - \frac{\Delta mg\Delta z}{RT_K} + \Omega\left(T_{(i)} - T_{(i-1)}\right)\right]}{\Delta z} + s_{o(i-0.5)}D_{eddy(i-0.5)}\frac{\left[\delta_{(i)} - \delta_{(i-1)}\right]}{\Delta z} \tag{A46}$$

$$j_{out} = -s_{o(i+0.5)}D_{mol(i+0.5)} \times \frac{\left[\delta_{(i+1)} - \delta_{(i)} - \frac{\Delta mg\Delta z}{RT_K} + \Omega\left(T_{(i+1)} - T_{(i)}\right)\right]}{\Delta z} + s_{o(i+0.5)}D_{eddy(i+0.5)}\frac{\left[\delta_{(i+1)} - \delta_{(i)}\right]}{\Delta z}. \tag{A47}$$

A third value of open porosity, corresponding to that of the grid point itself, is used for the calculation of the transport flux divergence and time derivative $\Delta\delta/\Delta t$:

$$\Delta\delta/\Delta t = [j_{in} - j_{out}]/\Delta z/s_{o(i)} \qquad \text{‰ s}^{-1} \tag{A48}$$

Table A2
List of symbol meanings

Symbol	Meaning
t	Time (s)
Δt	Time step (s)
z	Depth (m)
Δz	Grid spacing (m)
i, j	Grid index for numerical discretization (unitless integer)
δ	Fractional deviation of gas from standard (=[$q-1$] 10^3‰)
D_{mol}	Effective gas phase molecular diffusivity in firn ($m^2\ s^{-1}$)
D_{eddy}	Eddy diffusivity used to represent convective zone ($m^2\ s^{-1}$)
D_n	Diffusivity of gas n in ice lattice ($m^2\ s^{-1}$)
X_n	Solubility of gas n in ice lattice (mol m_{ice}^{-3} Pa^{-1})
x_n	Mole fraction of gas n in air (mol mol^{-1})
j_{in}, j_{out}	Transport model flux (in gas phase) (mol $m^{-2}\ s^{-1}$)
j_n	Permeation flux of gas n through ice lattice (mol $m^{-2}\ s^{-1}$)
J_n	Total permeation flux of gas n from a single bubble (mol s^{-1})
F_n	Bulk (aggregate) permeation flux of gas n per m^3 of firn (mol $m^{-3}\ s^{-1}$)
z_w	Bubble wall thickness (average) through which permeation occurs (m)
γ	Unknown constant relating to wall thickness (m)
A	Unknown constant for effective area of bubble wall (m^2)
N	Number of bubbles contributing to permeation flux (m^{-3})
T_K	Temperature (K)
p_n	Partial pressure of gas n (Pa)
P	Ambient barometric pressure (Pa)
Δm	Mass difference (e.g., 0.001 kg mol^{-1} for $^{15}N/^{14}N$)
g	Gravitational acceleration (9.82 m s^{-2})
R	Gas constant (8.314 J kg^{-1} mol^{-1})
Ω	Thermal diffusion sensitivity (‰ K^{-1}) [54,55]
R_{SA}	Sample gas ratio (mol mol^{-1}) (e.g., O_2/N_2, $^{15}N/^{14}N$)
R_{ST}	Standard gas ratio (mol mol^{-1})
R_{oe}	Ratio of enrichment of gas n/N_2 to O_2/N_2 (e.g., 34 for Ne)
q	Ratio of sample gas ratio to standard gas ratio ($\equiv R_{SA}/R_{ST}=\delta/10^3+1$)
s	Total porosity ($m^3\ m^{-3}$)
s_c	Closed porosity ($m^3\ m^{-3}$)
s_o	Open porosity ($m^3\ m^{-3}$)
Δs_c	Increment of closed porosity ($m^3\ m^{-3}$)
Δs_o	Increment of open porosity ($m^3\ m^{-3}$)
LID	Lock-in depth (m)
ρ	Bulk firn density (kg m^{-3})
ρ_{ice}	Real (temperature-dependent) ice density (kg m^{-3}) [52]
ρ_{LID}	Bulk density at lock-in horizon (kg m^{-3})
ΔV_b	Volume increment of air occluded in bubbles ($m^3\ m^{-3}$)
V_b	Integrated volume of air occluded in bubbles, at ambient pressure ($m^3\ m^{-3}$)
V_{bubble}	Average individual bubble volume (m^3) ($10^{-10}\ m^3$)
z_{layer}	Layer thickness in lock-in zone (m)
$E_{air(i)}$	Amount of air expelled from each layer in lock-in zone each year (mol m^{-2})
$\sum E_{air(i)}$	Total expulsion flux into each layer each year (mol m^{-2})
M_n	Inventory of gas n in a given reservoir (mol m^{-3})
δ_o	Gas composition in open pores (‰)
τ	Transit time for a firn particle to traverse a grid cell (s)
$\dot{b}$	Accumulation rate in ice equivalent (m s^{-1})
δ'	Updated value of δ (‰)
$\Delta\delta/\Delta t$	Time derivative of δ due to transport model fluxes (‰ s^{-1})

Combining both the old and new models, the open firn delta values δ_o are updated each time step according to:

$$\delta'_{o(i)} = [q'_{n(i)} - 1]10^3 + \Delta t(\Delta\delta/\Delta t) \quad ‰ \tag{A49}$$

where $\Delta t(\Delta\delta/\Delta t)$ is the transport flux term (note that $\Delta\delta$ only pertains to the change due to transport model fluxes).

A.7. Transition between open firn and lock-in models

At the lock-in horizon or LID, the two models are coupled synchronously. Once a year, when the lock-in zone values are computed, values from the deepest grid cell in the open firn q_{LID} are passed to the topmost layer in the lock-in zone. Based on the assumption that this layer seals off gradually, the average of beginning and ending values for the year is used. The time of year for updating the lock-in zone is chosen to be just prior to the time of firn air sampling to minimize artificial "step" offsets between the two models' values.

The air expelled from the lock-in zone is injected into the deepest grid cell in the open firn at each time step. This air is typically enriched in Ne, O_2 and Ar, and contributes slightly to the "uphole flux" of these gases to

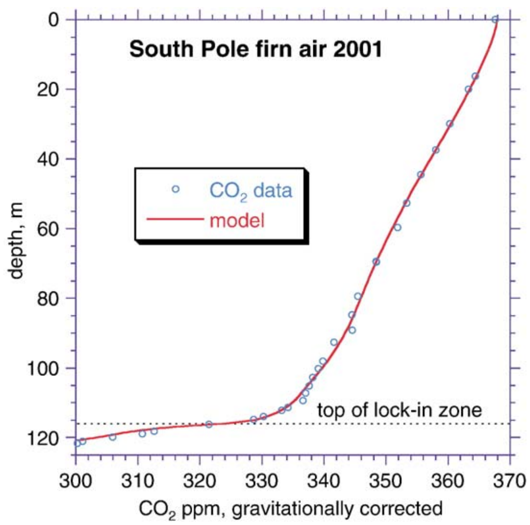

Fig. A4. Firn air CO_2 profile at South Pole, gravitationally corrected. The model was forced with the known atmospheric CO_2 history [24] (Fig. A6). Effective diffusivities as a function of depth were tuned to match the CO_2 data and these diffusivities are used in all subsequent runs. At any depth, the diffusivity of gas n divided by the diffusivity of CO_2 equals the ratio of free-air diffusivities. The depth of the lock-in zone was identified from this tuning procedure to be 116 m and is confirmed by $\delta^{15}N$ data (Fig. 2).

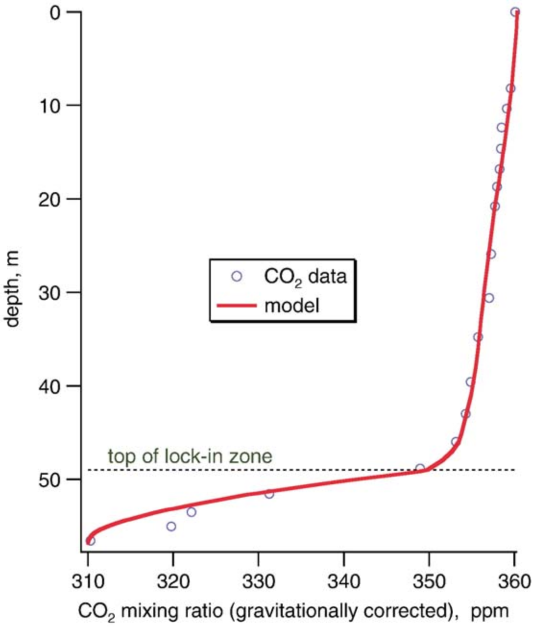

Fig. A5. Firn air CO_2 profile from Siple Dome, Antarctica, December 1996. Model curve was produced by adjusting firn effective diffusivity, with surface history from Law Dome ice core record [24]. Lock-in depth found by this process is 49 m.

the atmosphere [2]. The gas composition $q_{\mathrm{firnlockin}(2)}$ at the second layer in the lock-in zone is used to compute this flux, because the first layer has values that have just been passed from the open firn model. The first layer is also nearly at the same depth as the LID. The new inventory $M'_{n(\mathrm{firn})(\mathrm{LID})}$ in the bottommost grid cell of the open firn model is adjusted by:

$$M'_{n(\mathrm{firn})(\mathrm{LID})} = M'_{n(\mathrm{firn})(\mathrm{LID})} + x_{n(2)} \Sigma E_{\mathrm{air}(i)} / t_{\mathrm{a}} / \Delta z \Delta t \quad \mathrm{mol\ m^{-3}}. \tag{A50}$$

The fact that gas composition in the lock-in zone slightly affects gas composition in the open firn column and the open firn values are passed to the lock-in zone, suggest the existence of a feedback loop. For this reason, the model must be run for several decades before a steady state gas composition is reached in which the uphole flux balances the air injected from the lock-in zone.

An approximation to the advective bubble flux out of the bottom of the open firn model is used, because of the very different grid spacing in the lock-in zone (0.5 m for the open firn, ~0.1 m for the lock-in zone). The gradient in gas concentration is found from the bubble gas composition at a distance into the lock-in zone approximately equal to one firn model grid spacing. The layer number i corresponding to this distance is found from:

$$i = \mathrm{integer}[\Delta z / \dot{b} / t_{\mathrm{a}} \rho_{\mathrm{LID}} / \rho_{\mathrm{ice}}] \quad \text{unitless.} \tag{A51}$$

The average of $q_{\mathrm{firnbubble(LID)}}$ and $q_{\mathrm{lockinbubble}(i)}$ is then used to compute the bubble advective flux $J_{\mathrm{b(out)(LID)}}$ out of the bottommost cell in the open firn model as in (A40). Density and bubble volume at the underlying grid point (LID+1) are calculated in the model initialization.

A.8. Model validation

Ideally the model would be tested by comparison to direct measurements of closed porosity; unfortunately, direct measurements of closed porosity are not available at these sites to our knowledge. An indirect test of the model is that it should be able to produce realistic bubble gas composition and total air content in mature ice. As seen in Table A4, the model bubble $\delta^{15}N$ is in good agreement with observation when no mass-dependent close-off fractionation is included (further supporting the hypothesis of a sampling artifact to explain the lock-in $\delta^{15}N$ trend).

Model predictions of total air contents are within error of measured values for Siple Dome and South Pole

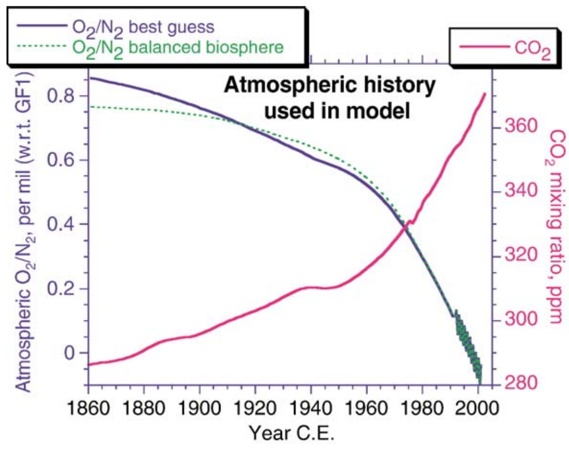

Fig. A6. Atmospheric histories used as an upper boundary condition for the model. CO_2 history is from the Law Dome ice core [24] and South Pole direct measurements [58]. O_2/N_2 histories prior to 1992 are computed from fossil fuel combustion data [59] for the "O_2 balanced biosphere" scenario, plus biospheric fluxes [60] for the "O_2 best guess" scenario. Stoichiometry for fossil fuel combustion is from [59] and stoichiometry for biospheric fluxes is −1.1 mol O_2/mol CO_2 [61]. The "O_2 best guess" scenario is used to force the model. After 1992, the South Pole direct measurement record is used (R. Keeling, written communication).

Table A3
Gas-specific parameters used in the model

		O_2	^{22}Ne	^{40}Ar	^{84}Kr	^{132}Xe	^{15}N	$^{28}N_2$	$^{40/36}$Ar	CO_2
Parameter										
Gas-phase diffusivity [a] in air relative to CO_2		1.27 [b]	1.89	1.21	0.93	0.80	1.25	–	1.21	1.00
Mass difference Δm (kg mol$^{-1}\times10^{-3}$)		4	−6	12	56	104	1	–	4	15
Thermal diffusion sensitivity [c]										
Ω (‰ K^{-1})		3.3 ^{15}N	−13 ^{15}N	16 ^{15}N	32 ^{15}N	35 ^{15}N	–	–	–	–
$\Omega = a/T_K - b/T_K^2$	a	–	–	–	–	–	8.656	–	26.08	–
	b	–	–	–	–	–	1232	–	3952	–
Permeability in ice DX [d]			23O_2							
Diffusivity (m^2 s^{-1})	D_o	3.50e−9						2.00e−10		
Activation energy (J mol^{-1})	Q	9700						5100		
$D = D_o \exp[Q/RT_K]$										
Solubility (Pa^{-1})	X_o	3.70e−13							4.50e−13	
Activation energy (J mol^{-1})	E	7900						9200		
$X = X_o \exp[E/RT_K]\rho_{ice}/(0.018$ kg mol$^{-1})$ (mol m$_{ice}^{-3}$ Pa^{-1})										
Mole fraction in air	0.20946	1.68e−6						0.7808		

[a] [35], except for O_2. Temperature and pressure corrections as in [13].
[b] [56].
[c] [13,33,54,55].
[d] [21], except for Ne, which is from this study.

(Table A4), although a bit low for Siple Dome. As mentioned above, the model has the simplification of maintaining ambient pressure in open pores, even in the lock-in zone. This is certain to bias the air content towards lower values; air in the open pores in the deeper part of the lock-in zone must be overpressured to some extent based on observed air content in ice [22]. During firn air experiments, we have observed ice crystals rising out of the borehole immediately after penetration of the lock-in zone, suggesting airflow out of the hole. This supports the notion that some air is overpressured in the lock-in zone. Also, it is possible that the discrepant air content could be due to a site-specificity in the closed porosity vs. density relation we used.

The major discrepancy between data and model is the high bubble O_2/N_2 predicted by the model (Table A4). Measurements of bubble O_2/N_2 from shallow ice cores (~130 m at South Pole and ~90 m at Siple Dome) show values about a factor of 4 more depleted in O_2 than predicted by the model. There are at least four possible explanations for this discrepancy.

First, postcoring losses of air through microcracks, in response to the abrupt pressure release upon core retrieval, might bias the observations of bubble O_2/N_2

Table A4
Observed vs. modeled bubble composition, uphole flux and air content

	South Pole		Siple Dome	
	Model	Measured	Model	Measured
Mean bubble δ^{15}N (‰)	+0.60	+0.61 ± 0.009 (n = 6) [a]	+0.22	+0.22 ± 0.002 (n = 20) [b]
With close-off fractionation	+0.58 [c]		+0.22 [c]	
Mean bubble $\delta O_2/N_2$ (‰) [d]	−2.01	−8.1 ± 0.4 (n = 6) [a]	−1.01	−4.3 ± 2.9 (n = 5) [b]
Alternative assumption [e]	−2.47		−1.69	
Uphole O_2 flux (mmol m^{-2} yr^{-1})	0.148		0.098	
Implied bubble O_2/N_2 (‰) [f]	−2.18		−0.89	
Total air content (ml$_{STP}$ kg^{-1})	96.0	92.5 ± 7 [g]	115	120 ± 10 [b]

[a] [2].
[b] Severinghaus (unpublished data).
[c] Arbitrary close-off fractionation imposed in order to fit observed lock-in firn air data.
[d] Corrected for anthropogenic and gravitational effects.
[e] Model bubble $\delta O_2/N_2$ based on the assumption that adjacent bubbles close off after a constant amount of closed porosity increase (0.1 of total closed volume), rather than a constant fraction of total porosity decrease.
[f] Calculated from uphole flux divided by mass accumulation rate, model total air content and O_2 mole fraction.
[g] From South Pole data presented in [22].

towards lower values [18]. Second, several studies [20,21] have documented a decline in O_2/N_2 over several years of sample storage time, implying that O_2 leaks out of bubbles in storage. Third, O_2 reacts with stainless steel surfaces and often loses 1–2‰ during extracted sample handling in the laboratory. However, these three possibilities do not explain the ~10‰ amplitude of insolation-linked O_2/N_2 variations in the deep Vostok [19] and Dome Fuji [20] cores.

A fourth possibility is that the model O_2/N_2 permeation fractionation is much too small. In trying to fit the model to the firn air data, we make the implicit assumption that the firn air observations represent an unbiased sampling of the average composition in open porosity. This assumption may be unrealistic. For example, it is likely that much of the open porosity is not accessible to a firn air experiment, but remains in sealed lenses. These lenses are large enough (several meters) that they are cut when closed porosity is measured on hand-samples. Thus they are not included in the definition of closed porosity. Therefore, it is possible that the layers actually sampled in a firn air study are exceptional layers with uncharacteristically high open porosity. These layers might be capable of delivering large volumes of air during sampling precisely because they are extraordinarily high in porosity. The extent of compositional evolution should be less in these layers than in the bulk, because the evolution is driven by fractional volume change (i.e., as in a Rayleigh distillation). Such a bias would produce unrealistically low values of the length scale obtained by fitting to the firn air O_2/N_2 data and unrealistically low gas loss and O_2/N_2 depletion.

One problem with this hypothesis, however, is that it also predicts that the model would severely underestimate the uphole flux of O_2 (by a factor of ~4). The good fit of the model to the firn air data in the 30 m above the lock-in zone is inconsistent with this prediction, unless our firn air diffusivities are badly wrong. It is unlikely that our diffusivities are a factor of 4 too low, as they are well constrained by the observed CO_2 data. As a check on the accuracy of our numerically deduced diffusivities, we solved a simplified diffusion model analytically and compared the numerical model result with the analytical solution. The analytical model is:

$$s_o \frac{\partial C}{\partial t} = \frac{\partial}{\partial z}\left[s_o D_{mol} \frac{\partial C}{\partial z}\right]. \tag{A52}$$

The surface forcing by the anthropogenic CO_2 increase was approximated by $C_{(o,t)} = [CO_2] - 288\,\text{ppm} = \exp(\mu t)$, where t (yr) = date − 1800 AD. The open porosity was approximated by $s_o = \nu z^2$, and the product of the open porosity and diffusivity by $s_o D_{mol} = \beta z^2$, z increasing upwards from 0.1 m at the bottom to 1 m at the surface. The analytical solution is:

$$C(z,t) = \exp(\mu t)\left[B_1 \frac{\sinh\left(\sqrt{\frac{\nu\mu}{\beta}}z\right)}{z} + B_2 \frac{\cosh\left(\sqrt{\frac{\nu\mu}{\beta}}z\right)}{z}\right] \tag{A53}$$

where B_1 and B_2 are constants determined by the boundary conditions. The numerical model was then run with identical boundary conditions, porosity and diffusivity. After a 200-yr integration, with $\mu = 0.022$, $\nu = 1$ and $\beta = 0.05$, the CO_2 concentration at the bottom boundary differed by only 0.01 ppm between analytical and numerical models. We take this agreement as confirmation that the numerical model is sufficiently accurate and hence the diffusivities obtained from CO_2 data are accurate and cannot be off by a factor of 4.

We also explored the possibility that the high model bubble O_2/N_2 could be due to a flawed assumption that permeation from a given bubble stops when the total porosity declines by a constant fraction (5%). Instead, we ran the model with the alternative assumption that permeation stops when the closed porosity increases by a constant amount (10% of the final air volume $V_{b(ice)}$). The value of 10% was chosen so that the model would still produce the same permeation fluxes in the lock-in zone and would therefore fit the lock-in zone firn air data, which are the strongest constraint. [This alternative assumption is physically plausible, in view of the fact that closure of the adjacent bubble should be directly related to an increase in closed volume.] This assumption has the result of shifting the distribution of permeation fluxes to slightly shallower depths, enhancing O_2 escape to the atmosphere. However, this alternative assumption only reduced bubble O_2/N_2 from −2.01‰ to −2.47‰ (Table A4). Therefore, the result is relatively insensitive to the specific assumption made regarding the duration of permeation flux from a single bubble.

Overall, these findings indicate that the observed uphole fluxes are inconsistent with the observed bubble O_2/N_2 of −8.1‰ at South Pole. Therefore, the disagreement is not really between our model and an observation, but rather between two different observations. As we cannot see how the uphole flux observations can be wrong, we conclude that it is likely that some artifactual loss of O_2 in the ice samples accounts for the factor of 4 discrepancy. Therefore, the true value of shallow bubble O_2/N_2 at South Pole is probably close to −2‰. This conclusion still leaves unexplained the insolation-linked deep ice core O_2/N_2 variations of ~10‰ [19,20], suggesting that our model is probably incapable of explaining these variations; however, we leave resolution of this puzzle to future work.

References

[1] J. Schwander, J.-M. Barnola, C. Andrie, M. Leuenberger, A. Ludin, D. Raynaud, B. Stauffer, The age of the air in the firn and the ice at Summit, Greenland, J. Geophys. Res. 98 (1993) 2831–2838.

[2] M. Battle, M.L. Bender, T. Sowers, P.P. Tans, J.H. Butler, J.W. Elkins, J.T. Ellis, T. Conway, N. Zhang, P. Lang, A.D. Clarke, Atmospheric gas concentrations over the past century measured in air from firn at the South Pole, Nature 383 (1996) 231–235.

[3] J.R. Petit, J. Jouzel, D. Raynaud, N.I. Barkov, J.-M. Barnola, I. Basile, M. Bender, J. Chappellaz, M. Davis, G. Delaygue, M. Delmotte, V.M. Kotlyakov, M. Legrand, V.Y. Lipenkov, C. Lorius, L. Pepin, C. Ritz, E. Saltzman, M. Stievenard, Climate and atmospheric history of the past 420,000 years from the Vostok ice core, Antarctica, Nature 399 (1999) 429–436.

[4] EPICA community members, Eight glacial cycles from an Antarctic ice core, Nature 429 (2004) 623–628.

[5] H. Craig, Y. Horibe, T. Sowers, Gravitational separation of gases and isotopes in polar ice caps, Science 242 (1988) 1675–1678.

[6] T. Sowers, M.L. Bender, D. Raynaud, Elemental and isotopic composition of occluded O_2 and N_2 in polar ice, J. Geophys. Res. 94 (1989) 5137–5150.

[7] J. Schwander, The transformation of snow to ice and the occlusion of gases, in: H. Oeschger, C.C. Langway Jr. (Eds.), The Environmental Record in Glaciers and Ice Sheets, John Wiley, New York, 1989, pp. 53–67.

[8] T. Sowers, M.L. Bender, D. Raynaud, Y.S. Korotkevich, $\delta^{15}N$ of N_2 in air trapped in polar ice: a tracer of gas transport in the firn and a possible constraint on ice age–gas age differences, J. Geophys. Res. 97 (1992) 15,683–15,697.

[9] J. Schwander, T. Sowers, J.-M. Barnola, T. Blunier, A. Fuchs, B. Malaize, Age scale of the air in the summit ice: implication for glacial–interglacial temperature change, J. Geophys. Res. 102 (1997) 19,483–19,493.

[10] N. Caillon, J.P. Severinghaus, J. Jouzel, J.-M. Barnola, J. Kang, V.Y. Lipenkov, Timing of atmospheric CO_2 and Antarctic temperature changes across Termination III, Science 299 (2003) 1728–1731.

[11] J.P. Severinghaus, A. Grachev, B. Luz, N. Caillon, A method for precise measurement of argon 40/36 and krypton/argon ratios in trapped air in polar ice with applications to past firn thickness and abrupt climate change in Greenland and at Siple Dome, Antarctica, Geochim. Cosmochim. Acta 67 (2003) 325–343.

[12] K.E. Grew, T.L. Ibbs, Thermal Diffusion in Gases, Cambridge Univ. Press, Cambridge, 1952.

[13] J.P. Severinghaus, A. Grachev, Battle, Thermal fractionation of air in polar firn by seasonal temperature gradients, Geochem. Geophys. Geosyst. 2 (2001) (paper number 2000GC000146, electronic journal).

[14] J.P. Severinghaus, T. Sowers, E.J. Brook, R.B. Alley, M.L. Bender, Timing of abrupt climate change at the end of the Younger Dryas interval from thermally fractionated gases in polar ice, Nature 391 (1998) 141–146.

[15] M.C. Leuenberger, C. Lang, J. Schwander, Delta ^{15}N measurements as a calibration tool for the paleothermometer and gas–ice age differences: a case study for the 8200 B.P. event on GRIP ice, J. Geophys. Res. 104 (1999) 22163–22170.

[16] A. Landais, N. Caillon, C. Goujon, A. Grachev, J.M. Barnola, J. Chappellaz, J. Jouzel, V. Masson-Delmotte, M. Leuenberger, Quantification of rapid temperature change during DO event 12 and phasing with methane inferred from air isotopic measurements, Earth Planet. Sci. Lett. 225 (2004) 221–232.

[17] J.P. Severinghaus, E.J. Brook, Abrupt climate change at the end of the last glacial period inferred from trapped air in polar ice, Science 286 (1999) 930–934.

[18] M.L. Bender, T. Sowers, V. Lipenkov, On the concentration of O_2, N_2, and Ar in trapped gases from ice cores, J. Geophys. Res. 100 (1995) 18,651–18,660.

[19] M.L. Bender, Orbital tuning chronologies for the Vostok climate record supported by trapped gas composition, Earth Planet. Sci. Lett. 204 (2002) 275–289.

[20] K. Kawamura, Variations of atmospheric components over the past 340000 years from Dome Fuji deep ice core, Antarctica, PhD thesis, Tohoku University, 2000, 216 pp.

[21] T. Ikeda-Fukazawa, K. Fukumizu, K. Kawamura, S. Aoki, T. Nakazawa, T. Hondoh, Effects of molecular diffusion on trapped gas composition, Earth Planet. Sci. Lett. 229 (2005) 183–192.

[22] P. Martinerie, D. Raynaud, D.M. Etheridge, J.-M. Barnola, D. Mazaudeir, Physical and climatic parameters which influence the air content of polar ice, Earth Planet. Sci. Lett. 112 (1992) 1–13.

[23] D.M. Etheridge, G.I. Pearman, P.J. Fraser, Changes in tropospheric methane between 1841 and 1978 from a high accumulation-rate Antarctic ice core, Tellus 44B (1992) 282–294.

[24] D.M. Etheridge, L.P. Steele, R.L. Langenfields, R.J. Francey, J.-M. Barnola, V.I. Morgan, Natural and anthropogenic changes in atmospheric CO_2 over the last 1000 years from air in Antarctic ice and firn, J. Geophys. Res. 101 (1996) 4115–4128.

[25] M.L. Bender, T. Sowers, J.-M. Barnola, J. Chappellaz, Changes in the O_2/N_2 ratio of the atmosphere during recent decades reflected in the composition of air in the firn at Vostok Station, Antarctica, Geophys. Res. Lett. 21 (1994) 189–192.

[26] M.L. Bender, P.P. Tans, J.T. Ellis, J. Orchardo, K. Habfast, A high-precision isotope ratio mass-spectrometry method for measuring the O_2/N_2 ratio of air, Geochim. Cosmochim. Acta 58 (1994) 4751–4758.

[27] M.L. Bender, D.T. Ho, M.B. Hendricks, R. Mika, M.O. Battle, P. P. Tans, T.J. Conway, B. Sturtevant, N. Cassar, Atmospheric O_2/N_2 changes, 1993–2002: implications for the partitioning of fossil fuel CO_2 sequestration, Glob. Biogeochem. Cycles 19 (2005) GB4017.

[28] W.S.B. Paterson, The Physics of Glaciers, third edition, Pergamon, New York, 1994.

[29] V.Y. Lipenkov, A.N. Salamatin, P. Duval, Bubbly-ice densification in ice sheets: II. Applications, J. Glaciol. 43 (1997) 397–407.

[30] S.C. Colbeck, Air movement in snow due to windpumping, J. Glaciol. 35 (1989) 209–213.

[31] A. Fabre, J.-M. Barnola, L. Arnaud, J. Chappellaz, Determination of gas diffusivity in polar firn: comparison between experimental measurements and inverse modeling, Geophys. Res. Lett. 27 (2000) 557–560.

[32] C.M. Trudinger, I.G. Enting, D.M. Etheridge, R.J. Francey, V.A. Levchenko, L.P. Steele, D. Raynaud, L. Arnaud, Modeling air movement and bubble trapping in firn, J. Geophys. Res. 102 (1997) 6747–6763.

[33] B. Nemzer, J.P. Severinghaus, Thermal diffusion constants of noble gases in air for paleoenvironmental applications (in preparation).

[34] J.P. Severinghaus, M. Battle, Ninety per mil enrichment of neon in firn air at South Pole, Geophys. Res. Abstr. 4 (2002) (EGS02-A-00510).

[35] R.C. Reid, J.M. Prausnitz, B.E. Poling, The Properties of Gases and Liquids, fourth edition. McGraw-Hill, New York, 1987.

[36] M. Albert, E. Shultz, F. Perron, Snow and firn permeability at Siple Dome, Antarctica, Ann. Glaciol. 31 (2000) 353–356.

[37] M.M. Herron, C.C. Langway, Firn densification: an empirical model, J. Glaciol. 25 (1980) 373–385.

[38] H. Craig, R.C. Wiens, Gravitational enrichment of $^{84}Kr/^{36}Ar$ ratios in polar ice caps: a measure of firn thickness and accumulation temperature, Science 271 (1996) 1708–1710.

[39] M.A. Headly, J.P. Severinghaus, Reconstructing deep ocean temperature during the last glacial maximum based on Kr/N_2 and Xe/N_2 ratios in air trapped in glacial ice, Eos Trans. AGU 85 (47) (2004) (Fall Meet. Suppl., PP23B-1409).

[40] R.F. Keeling, A.C. Manning, E.M. McEvoy, S.R. Shertz, Methods for measuring changes in atmospheric O_2 concentration and their application in southern hemisphere air, J. Geophys. Res. 103 (1998) 3381–3397.

[41] P. Jean-Baptiste, J.-R. Petit, V.Y. Lipenkov, D. Raynaud, N.I. Barkov, Constraints on hydrothermal processes and water exchange in Lake Vostok from helium isotopes, Nature 411 (2001) 460–462.

[42] K. Satoh, T. Uchida, T. Hondoh, S. Mae, Diffusion coefficient and solubility measurements of noble gases in ice crystals, Proc. NIPR Symp. Polar Meteorol. Glaciol. 10 (1996) 73–81.

[43] T. Ikeda-Fukazawa, K. Kawamura, T. Hondoh, Mechanism of molecular diffusion in ice crystals, Mol. Simul. 30 (2004) 973–979.

[44] C. Huber, U. Beyerle, M. Leuenberger, J. Schwander, R. Kipfer, R. Spahni, J. Severinghaus, K. Weiler, Evidence for molecular size dependent gas fractionation in firn air derived from noble gases, oxygen, and nitrogen measurements, Earth Planet. Sci. Lett. (in press).

[45] J. Kärger, D.M. Ruthven, Diffusion in Zelolites and other Microporous Solids, John Wiley and Sons, Inc., New York, 1992.

[46] J.P. Severinghaus, Annual layering of gas ratios in ice cores, Proceedings of Chapman Conference: Mechanisms of Millennial Scale Climate Change, Snowbird, Utah, June 14–18, 1998, American Geophysical Union, 1998, p. 25.

[47] E.M. Hood, Characterization of air–sea gas exchange processes and dissolved gas/ice interactions using noble gases, Ph.D. Thesis, MIT/WHOI, 1998, 266 pp.

[48] L. Machta, E. Hughes, Atmospheric oxygen in 1967 to 1970, Science 168 (1970) 1582–1584.

[49] R.F. Keeling, S.R. Shertz, Seasonal and interannual variations in atmospheric oxygen and implications for the global carbon cycle, Nature 358 (1992) 723–727.

[50] R.F. Keeling, S.C. Piper, M. Heimann, Global and hemispheric CO_2 sinks deduced from changes in atmospheric O_2 concentration, Nature 381 (1996) 218–221.

[51] M.L. Bender, J.T. Ellis, P.P. Tans, R.J. Francey, L.D., Variability in the O_2/N_2 ratio of southern hemisphere air, 1991–1994: implications for the carbon cycle, Glob. Biogeochem. Cycles 10 (1996) 9–21.

[52] H. Bader, Density of ice as a function of temperature and stress, CRREL Spec. Rep., vol. 64, Cold Regions Research and Engineering Laboratory, Hanover, N.H., 1964

[53] J. Crank, The Mathematics of Diffusion, Second edition, Clarendon Press, Oxford, 1975.

[54] A.M. Grachev, J.P. Severinghaus, Determining the thermal diffusion factor for $^{40}Ar/^{36}Ar$ in air to aid paleoreconstruction of abrupt climate change, J. Phys. Chem., A 107 (2003) 4636–4642.

[55] A.M. Grachev, J.P. Severinghaus, Laboratory determination of thermal diffusion constants for $^{29}N_2/^{28}N_2$ in air at temperatures from -60 to $0\,°C$ for reconstruction of magnitudes of abrupt climate changes using the ice core fossil–air paleothermometer, Geochim. Cosmochim. Acta 67 (2003) 345–360.

[56] J. Schwander, B. Stauffer, A. Sigg, Air mixing in firn and the age of the air at pore close-off, Ann. Glaciol. 10 (1988) 141–145.

[57] K.C. Taylor, J.W.C. White, J.P. Severinghaus, E.J. Brook, P.A. Mayewski, R.B. Alley, E.J. Steig, M.K. Spencer, E. Meyerson, D.A. Meese, G.W. Lamorey, A. Grachev, A.J. Gow, B.A. Barnett, Abrupt climate change around 22 ka on the Siple Coast of Antarctica, Quat. Sci. Rev. 23 (2004) 7–15.

[58] C.D. Keeling, T.P. Whorf, Atmospheric CO_2 records from sites in the SIO air sampling network, Trends: A Compendium of Data on Global Change, Carbon Dioxide Information Analysis Center, Oak Ridge National Laboratory, U.S. Department of Energy, Oak Ridge, TN, USA, 2004.

[59] R.F. Keeling, Development of an interferometric oxygen analyzer for precise measurement of the atmospheric O_2 mole fraction, Ph.D. dissertation, Harvard Univ., Cambridge, MA, 1988, 179 pp.

[60] M. Bruno, F. Joos, Terrestrial carbon storage during the past 200 years: a Monte Carlo analysis of CO_2 data from ice core and atmospheric measurements, Glob. Biogeochem. Cycles 11 (1997) 111–124.

[61] J.P. Severinghaus, Studies of the terrestrial O_2 and carbon cycles in sand dune gases and in Biosphere 2, Ph.D. dissertation, Columbia Univ., New York, 1995, 148 pp.